5-2013

Synthesis and Characterization of Iron Pyrite Nanocrystals for Photovoltaic Devices

Scott Curtis Mangham
University of Arkansas, Fayetteville

SYNTHESIS AND CHARACTERIZATION OF IRON PYRITE NANOCRYSTALS FOR PHOTOVOLTAIC DEVICES

Synthesis and Characterization of Iron Pyrite Nanocrystals for Photovoltaic Devices

A thesis submitted in partial fulfillment
of the requirements for the degree of
Master of Science in Electrical Engineering

By

Scott Curtis Mangham
Lamar University
Bachelor of Science in Electrical Engineering, 2010

May 2013
University of Arkansas

Abstract

Iron pyrite nanocrystals have been synthesized using a hot-injection method with a variety of amines and characterized with properties necessary for photovoltaic devices. The iron pyrite nanocrystals were characterized using X-ray diffraction, scanning electron microscopy, transmission electron microscopy, optical absorption, micro-Raman, and micro-Photoluminescence. The optical absorbance spectra showed the large absorption in the visible and near infrared spectral range for the nanocrystals as well as to show the band gap. The face-centered cubic crystal structure of the iron pyrite nanocrystals was shown by matching the measured X-ray diffraction pattern to a face-centered cubic iron pyrite reference pattern. Using Bragg's law and Scherrer's formula helps to calculate the grain size and lattice spacing based upon the X-ray diffraction pattern. The scanning electron microscopy produces images that show the particle size of the nanocrystals while the transmission electron microscopy produced images that show the lattice spacing and grain size for the iron pyrite nanocrystals that are compared to the previously mentioned calculated grain size and lattice spacing. The micro-Raman and micro-Photoluminescence are used to compare the synthesized iron pyrite nanocrystals to natural-bulk iron pyrite. The micro-Photoluminescence is also used to calculate a band gap and compare this band gap to the one obtain by the optical absorbance spectra.

This thesis is approved for recommendation
to the Graduate Council.

Thesis Director:

_____

Dr. Omar Manasreh

Thesis Committee:

_____

Dr. Simon Ang

_____

Dr. Magda El-Shenawee

_____

Dr. Mahmood Alam Khan

Thesis Duplication Release

I hereby authorize the University of Arkansas Libraries to duplicate this thesis when needed for research and/or scholarship.

Agreed _____

Scott Curtis Mangham

Refused _____

Scott Curtis Mangham

Acknowledgments

I would like to thank my chair advisor and project director, Dr. Omar Manasreh for his support and guidance throughout my years at the University of Arkansas as well as his knowledge that has helped to focus my research. I am grateful to the members of my committee, Dr. Simon Ang, Dr. Magda El-Shenawee, and Dr. Mahmood Alam Khan, for being a part of my thesis committee and their valuable support and guidance towards the completion of my thesis. Dr. Mahmood Alam Khan has been beneficial as he has helped me to learn to perform many crucial aspects of the experiment. The support granted by both the Air Force Office of Scientific Research (Grant no. FA9550-10-1-0136), the NSF-EPSCoR Program (Grant no. EPS-1003970), and NASA (Grant no. 242026-1BBX11AQ36A) has been invaluable throughout my time at the University of Arkansas.

I would also like to express my thanks to my research colleagues, Dr. Scott Little, Seungyong Lee, Rick Eyi, Dr. Jiang Wu, David Fryauf, Ramesh Vasaan, Jony Sarker, Ahmad Ibrahim Mohammad Nusir, Juan Aguilar, Zach Bever, Yahia Makableh, and William Wilson for all their help, both in class work as well as in conducting experiments.

Lastly, and most importantly I would like to thank my family for their constant support throughout my education. The love and support provided from my parents, grandparents, siblings, and extended family has been a true blessing in encouraging me throughout.

Table of Contents

Table of Figures

Table of Tables

Abbreviations

EDX – Energy-dispersive X-ray spectroscopy

eV – Electron Volt

FeS – Troilite

FeS_2 – Iron Pyrite, Iron(II) Disulfide

$Fe_{1-x}S_x$ – Pyrrhotite

GaAs – Gallium Arsenide

NaCl – Sodium Chloride, Salt, Halite

PL – Photoluminescence

S_2 – Disulfur

SEM – Scanning Electron Microscope

Si – Silicon

TEM – Transmission Electron Microscope

TOPO – Trioctylphosphine Oxide

UV-Vis – Ultraviolet-Visible

UV-Vis-NIR – Ultraviolet-Visible-Near Infrared

XRD – X-ray diffraction

1. Introduction

Iron pyrite (FeS_2) has been a material investigated recently due to the optical properties and cost of the material lending itself greatly for photovoltaic devices. The optical properties of the iron pyrite are promising for photovoltaic devices due to the reported indirect band gap of 0.95 eV, direct band gap of 1.03 eV, suitable light absorption coefficient of $10^4\ cm^{-1}$ for the band gap of 0.95 eV, high electron mobility of $230\ cm^2\ V^{-1}S^{-1}$, the minority carrier diffusion length of $100-1000\ nm$, and the vast availability of the material [1]-[20]. The availability of the material helps lower the cost of the iron pyrite to a significantly lower material extraction cost than a large portion of the other materials investigated for photovoltaic devices. The properties and cost of iron pyrite could eventually prove to be a practical method of producing solar energy. One of the main properties necessary for creating photovoltaic is the ability to absorb a considerable portion of the solar spectrum. There have been different materials capable of performing this feat from crystalline silicon, to amorphous silicon, and also gallium arsenide (GaAs). While the efficiencies of Si and GaAs have made significant strides towards approaching a theoretical maximum, iron pyrite has yet to exhibited 5% efficiency, despite the band gap of iron pyrite leads to a maximum theoretical efficiency of well over 20% [14].

The low material cost of iron pyrite is due in part to the abundant and widespread nature of the material and because of the iron pyrite being associated with valuable minerals and materials, such as sphalerite, chalcopyrite, galena, and gold [8],[10]. This abundant nature and association with other materials has led to the perception of iron pyrite being a waste material that has to be separated by an expensive procedure, with some of the procedures being either leaching or flotation. It has also been instrumental in causing acid rock damage that cost the

mining industry more than $1 million per day [8]. These factors have help lead to the material extraction cost of silicon being more than 20,000 times the material extraction cost for iron pyrite [9].

1.1 Structure of Iron Pyrite

The structure of iron sulfide can exist in a variety of forms that include FeS, $Fe_{1-x}S_x$, and FeS_2. The crystal structure of FeS is of a troilite, the $Fe_{1-x}S_x$ exhibits a pyrrhotite, and the FeS_2 can be of a marcasite or pyrite structure [21]. While all three of the forms are iron sulfides, only the iron pyrite exhibiting a face-centered cubic crystal structure has the desired attributes. One of the reasons that FeS and $Fe_{1-x}S_x$ is not a desired crystal structure is due to FeS having a 0.04 eV band gap while $Fe_{1-x}S_x$ has a 0.2 eV band gap. Considering a desirable band gap range of 0.9 to 1.7 eV is necessary for achieving a maximum efficiency percentage of at least 28%, the crystal structure of pyrrhotite and troilite would be undesirable [22]. Because of the adverse band gap of the FeS and $Fe_{1-x}S_x$ highlights the need to have a material that is purely FeS_2.

Within FeS_2 there are two possible crystal structures, the pyrite and marcasite structure. The pyrite is a face-centered cubic crystallographic structure while the marcasite is an orthorhombic structure. Marcasite is considered to be a less stable structure that has a band gap of 0.34 eV that is undesirable for photovoltaic devices [5],[8]. Because of the possibility of the marcasite structure existing within FeS_2 alongside the pyrite and degrading the optical properties of the FeS_2 leading to a poly-phase device rather than the desired phase-pure device. The face-centered cubic iron pyrite is one of the most common of the sulfide minerals that has a structure in the same vein as NaCl. The face-centered cubic iron pyrite is structured by having the Fe atoms on both the corners and the center of the faces of the structure while the S_2 dumbbell

shaped atoms are located midpoint of the edges as well as the absolute center of the cube [24]. The aforementioned face-centered cubic structure for the iron pyrite is shown in Fig. 1.1.

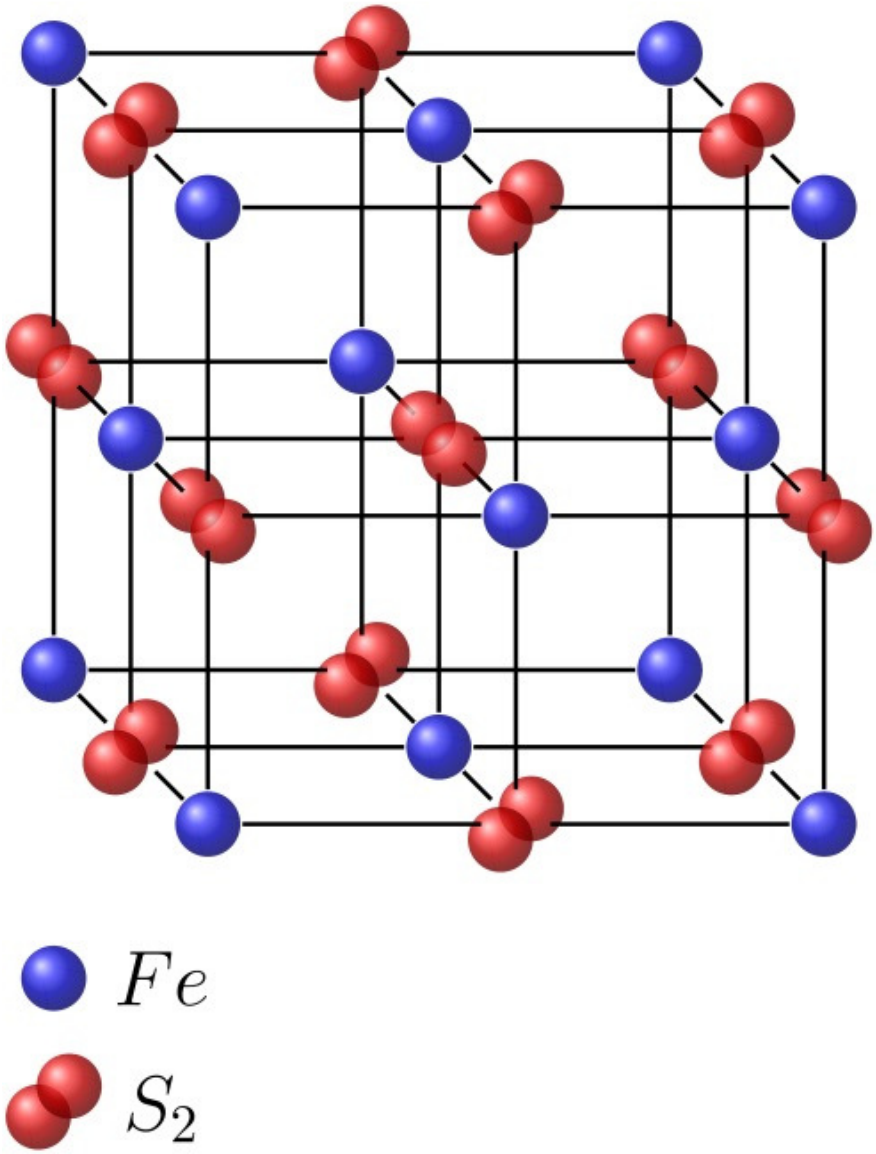

Fig. 1.1. Above is the crystal structure of face-centered cubic iron pyrite with one atom of iron (Fe) on each corner and face of the cube and the two atoms of sulfur (S_2) is on each edge of the cube as well as in the center of the cube.

1.2 Optical Properties of Iron Pyrite

The optical properties of iron pyrite have been shown to have a suitable band gap, high

optical absorption coefficient, and high electron mobility that can be either an n-type or p-type semiconductor material [8],[23]. The band gap of iron pyrite has been widely reported with having an indirect band gap of 0.95 eV while also having a direct band gap of 1.03 eV [1]-[20]. There has been a slight range in the indirect band gap that has been reported to be from 0.8 to 1.1 eV however, the majority exhibits the 0.95 eV for the indirect band gap that has been widely reported [14]. An integrated absorption coefficient ranging from 10^4 to 3.3×10^5 cm^{-1} for the wavelength range of 300 to 750 nm has been reported that helps the iron pyrite have strong absorption within the visible region of the solar spectrum [10],[14],[25]. Having high electron mobility in the iron pyrite is beneficial due to the exciton dissociation rate depending on the mobility in potential photovoltaic devices [26].

1.3 Synthesis Methods

To synthesize iron pyrite there have been several methods that include surfactant assisted hot-injection method, metal-organic chemical vapor deposition, thermal sulfidation of iron, chemical vapor transport, electrodeposition, and facile synthesis [5],[13],[15],[21]. Each method has been utilized to create a different type of iron pyrite, from creating a thin film, to nanocrystals, and all the way to bulk iron pyrite. The hot-injection method, also referred to as the colloidal or pyrolytic method, was chosen to investigate due to the capabilities to produce phase-pure nanocrystals that can be scaled up to mass production levels.

There have been several variations of the hot-injection method, but the basic premise has been to create one solution, A, and to inject A into a second solution, B, at an elevated temperature followed by stirring for a pre-determined amount of time to create a new solution, AB. This AB is then purified by a chloroform and ethanol mixture. To separate the desired

nanocrystals from the rest of the solution a centrifuge with additional chloroform is used. This process removes the undesired residual products as well as larger nanocrystals than preferred.

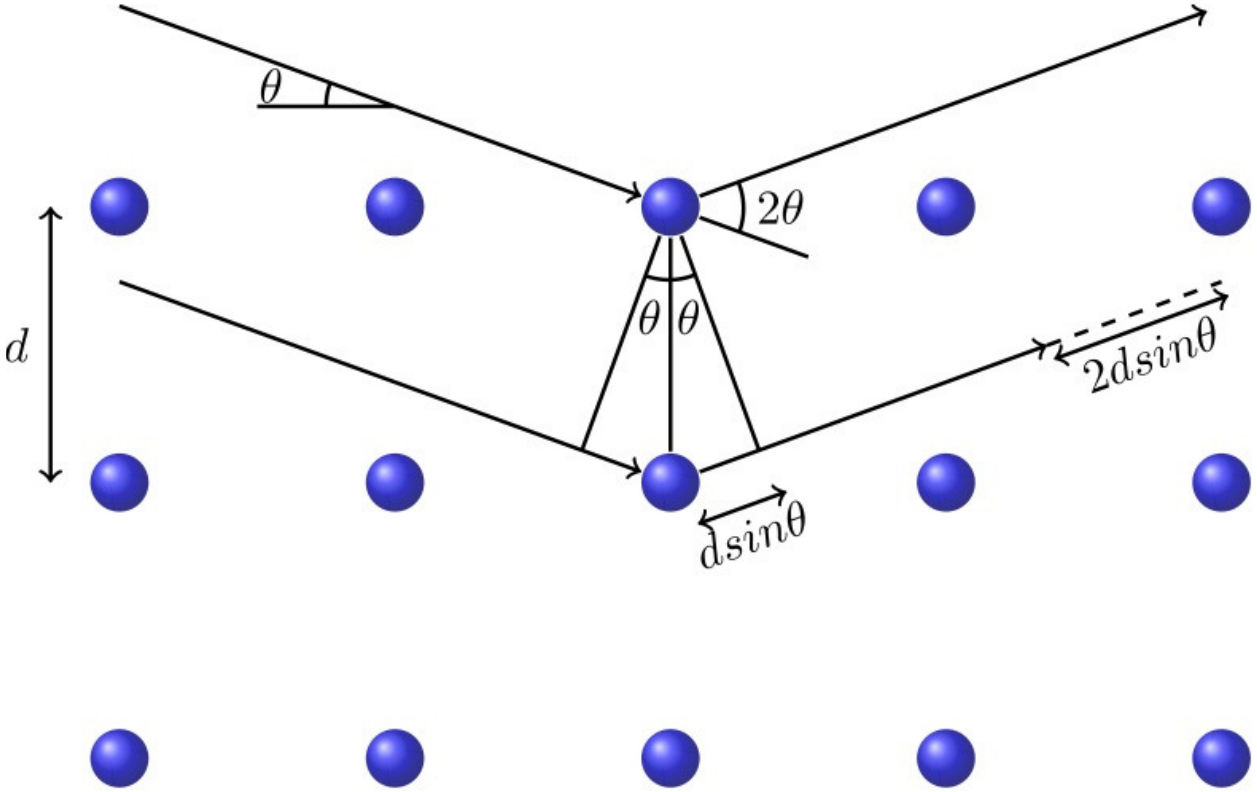

Fig. 1.2. Two X-ray beams with identical wavelength and phase approach a sample and scatter off of two different atoms within the sample. The lower beam travels a distance greater than the upper beam by a distance of $2d\sin(\theta)$.

1.3.1 Advantages of the Hot-Injection Method

Some of the advantages of the hot-injection method is the ability to have fairly quick nucleation, highly accurate and precise particle size control, and the high temperature can help lead to quality crystal structure. There is also the added benefit of the lack of toxic or expensive chemicals used in the hot-injection method for the purpose of synthesizing iron pyrite nanocrystals. The quick nucleation is caused because of the injection of a room temperature

precursor into a hot liquid, normally a solvent. After the injection into the hot liquid, there is the formation of nuclei and to prevent the formation of new nuclei afterwards, the solution is then cooled down. For size control, the solution is heated to less than 300°C to allow for the existing nuclei to grow while preventing the formation of nuclei occurring. The chosen temperature to heat the solution up to is one of the determining factors to the size of the resulting nanocrystals [27]. By controlling the formation of new nuclei, and controlling the temperature and time variables, the resulting nanocrystals will be of similar sizes and shapes. This same process should also be able to be scaled up for larger scale production of iron pyrite nanocrystals.

1.4 Characterization Techniques

Characterization of the iron pyrite nanocrystals was performed using an ultraviolet-visible (UV-Vis) optical spectrometer, X-ray diffraction (XRD), scanning electron microscope (SEM), energy-dispersive X-ray spectroscopy (EDX), and a transmission electron microscope (TEM). A Varian Cary 500 UV-Vis-NIR spectrophotometer was used to measure the optical absorption, for the measurement of the XRD spectrum a Philips PW3040 X'Pert MRD High Resolution XRD was used, to produce the SEM images and the EDX spectra a FEI Nova Nanolab 200 Dual-Beam Focused Ion Beam with a FEG Scanning Electron Microscope was used, and a FEI Titan 80-300 Transmission Electron Microscope produced the TEM images.

$$A = -\log(T) = -\log\left(\frac{I}{I_0}\right) \tag{1.1}$$

The UV-Vis optical spectrometer has the capabilities of measuring the absorption, transmission, and the reflection for a given wavelength range. For the purpose of iron pyrite the absorption has been measured to test the range of wavelength the material can absorb. This has the benefit of also being able to deduce the band gap of the material measured based upon the

absorption edge characteristics. The absorption (A) is measured based upon the transmission (T) of the light that passes through the material, with the transmission being equivalent to the ratio of the transmitted light intensity (I) to the incident light intensity (I_0). The equation for absorption is shown in equation (1.1) directly above this paragraph. Measured absorption spectra are also useful for displaying the absorption at a given wavelength and this can help to show if the material is capable of absorbing light in the visible spectrum.

$$2d\sin(\theta) = n\lambda \tag{1.2}$$

$$\tau = \frac{K\lambda}{\beta\cos(\theta)} \tag{1.3}$$

The XRD pattern is based upon Bragg's law, also referred to as the Bragg formulation of X-ray diffraction and shown in equation (1.2), which was first proposed in 1913. Where the wavelength for the X-ray beam (λ) is used to help determine the distance (d) between the atomic layers in the crystal with the angle of incidence (θ) based upon the reflection of the incoming X-ray beam. This basic principle helps to formulate the XRD spectrum for the individual angles based upon a given λ. In Fig. 1.2 the incident of two identical X-rays with identical wavelength and phase is shown interacting with a sample, with the lower X-ray traveling $2d\sin(\theta)$ more than the upper X-ray. Bragg's law can also be used to take the resulting XRD spectrum and calculate the lattice spacing of the sample. The Scherrer Formula is shown in equation (1.3) and is used to calculate the grain size of the sample based upon the XRD spectrum where K is the shape factor, λ is the wavelength of the X-ray, β is the full width at half maximum of a given peak, θ is the Bragg angle, and τ is the linear dimension of the particle [28].

A SEM is a type of electron microscope that refracts and focuses an ion beam. By scanning this focused ion beam across a sample and reading the interaction between the electrons

from the ion beam and the electrons in the sample to produce an image of the sample that displays information about the shape of the particles, which includes the dimensions of the particles. Due to some of the limitations of the SEM it is unable to detect the individual grain size, and it produces images that focus more on the, relatively speaking, macro scale rather than the micro scale that could potentially show the individual grain size or the lattice spacing. This need of a technique to show more detail leads to the inclusion of the TEM. The resolution of the TEM allows the examination of fine details of a sample to the point that the visibility of single columns of atoms can become accessible, and with this data the information about lattice spacing and the individual grain size becomes apparent. This information is useful in comparing the grain size to the calculated grain size obtained by the Scherrer formula using the XRD spectrum and the lattice spacing can be used to compare to both the calculated lattice spacing from Bragg's law and reference material.

A HORIBA Scientific LabRAM HR was used to measure the micro-Raman spectrum and the micro Photoluminescence (PL) of the sample with the ability to measure with different lasers throughout the UV-Vis-NIR range. The Raman spectroscopy will be able to help to identify what material is being examined, and whether it is a phase-pure material because it can identify the different peaks produced by various molecules. This is possible because of the difference in molecules atomic masses and the strength of the bonds between the atoms that lead to identifiable peaks. Along with XRD spectrum, this technique can confirm that the material has been measured to be a particular material. The micro-PL is able to demonstrate the optoelectronic properties of a given material by showing the ability to absorb and re-radiate photons due to the excitation of electrons. Both micro-PL and PL are routinely used to

characterize various semiconductor materials due to the non-destructive nature of the technique and the various characterizations of the material made apparent due to the PL.

2. Experiment Setup

The goal of the synthesis was to grown iron pyrite that is devoid of any organic surfactant or multi-solvents. This has been achieved by first synthesizing and optimizing the synthesis temperature conditions for iron pyrite with octylamine and dipenhyl ether to create phase-pure iron pyrite. The next stage consisted of removing the dipenhyl ether ink the sulfur precursor and replacing it with octylamine as well as an inclusion of the organic surfactant TOPO in the iron precursor. For the following stage the removal of the TOPO was necessary to try to exclude the usage of a surfactant due to the possibility of a surfactant being a hindrance in potential device efficiencies. The last stage was to remove the octylamine in favor of oleylamine due to the ability of oleylamine to dissolve in different solvents.

2.1 Synthesis Method for Iron Pyrite

A hot injection method was utilized to prepare the face-centered cubic iron pyrite nanocrystals using a variety of surfactants and solvents. To prepare the face-centered cubic iron pyrite nanocrystals the equipment consisted of two different three-necked Schlenk flask, with one of the flask used to prepare the iron precursor and the other prepare the sulfur precursor. The iron precursor was prepared by combining 10 mL of octylamine (Aldrich) with 2.5 mmol of $FeCl_2.4H_2O$ (Alfa Aesar) in a N_2 rich environment in one of the three-necked Schlenk flask. This mixture was mildly stirred at 115°C for 1 ½ hours to degas the mixture. For the sulfur precursor, a mixture of 500 mg of Sulfur (Aldrich) was mixed in 15 mL of diphenyl ether and degassed in another N_2 rich environment at 85°C for 1 hour. The iron precursor is then increased

in temperature until it reaches a desired temperature that has been declared as the main variable as the following temperatures have been used, 175°C, 215°C, 230°C, 240°C, and 260°C. With the iron precursor heated to the desired temperature the sulfur precursor is injected into the Schlenk flask containing the iron precursor where this reaction is carried out for 2 hours while continuously stirring vigorously. After 2 hours have elapsed and the temperature has cooled to 85°C, a few drops of chloroform (Aldrich) are added to prevent coagulation. The final step is to wash the solution with methanol three times in a HERMLE Z300 centrifuge at 5000 rpm for 10 minutes. The steps involved with cooling the solution, the adding of the chloroform, and the cleaning with the methanol using the centrifuge is repeated as the final step regardless of the method used for the iron or sulfur precursor, and neither does the synthetic temperature have a bearing on this final step.

After discovering the optimal temperature for nanocrystals growth the next step is to adjust the chemicals used in the preparation of the sulfur precursor while the iron precursor used the same method. The sulfur precursor is made by using 500 mg of Sulfur and mixing it with 15 mL of octylamine. This mixture is then degassed in a N_2 rich environment at 85°C for 1 hour. The iron precursor is heated until 230°C with the sulfur precursor then injected into the iron precursor and vigorously stirred for 2 hours. This is followed by the standard last step to produce the nanocrystals.

The next part of the experiment was to introduce the surfactant TOPO into the sulfur precursor. This was done by first creating the sulfur precursor as normal by using 500 mg of Sulfur and mixing it with 15 mL of octylamine followed by being degassed in a N_2 rich environment at 85°C for 1 hour. This is followed by the inclusion of the surfactant TOPO by

adding 2.0 mmol of TOPO (Aldrich) into the sulfur precursor and stirring until the surfactant has been dissolved. The iron precursor began the same by combining the 10 mL of octylamine with 2.5 mmol of $FeCl_2.4H_2O$ in a N_2 rich environment that was mildly stirred for 1 ½ hours at 115°C to degas the mixture. This iron precursor was then heated to 230°C; afterwards the sulfur precursor with TOPO was injected into the iron precursor and stirred vigorously for 2 hours. This is followed by the standard last step to clean and produce the nanocrystals.

Sulfur Precursor Ingredients	Iron Precursor Ingredients	Synthetic Temperature
500 mg Sulfur 15 mL Diphenyl Ether	10 mL Octylamine 2.5 mmol $FeCl_2.4H_2O$	175°C, 215°C, 230°C, 240°C, and 260°C
500 mg Sulfur 15 mL Octylamine	10 mL Octylamine 2.5 mmol $FeCl_2.4H_2O$ 2.0 mmol TOPO	230°C
500 mg Sulfur 15 mL Octylamine	10 mL Octylamine 2.5 mmol $FeCl_2.4H_2O$	230°C
500 mg Sulfur 15 mL Oleylamine	10 mL Oleylamine 2.5 mmol $FeCl_2.4H_2O$	230°C

Table 2.1. The first column is the ingredients in the sulfur precursor while the second column details the ingredients in the iron precursor. The third column displays the synthetic temperature for creating the nanocrystals. Each row details a stage in the experiment to synthesize the phase-pure iron pyrite nanocrystals.

The final part of the experiment was to remove the TOPO, octylamine, and the diphenyl ether in favor of using oleylamine for both the sulfur and the iron precursors. This was accomplished by making the sulfur precursor by using 500 mg of Sulfur and mixing it with 15 mL of oleylamine (Aldrich). The mixture is then degassed in a N_2 environment while being heated to 85°C and being continuously stirred for 1 hour. For the iron precursor there was a combination of 10 mL of oleylamine with 2.5 mmol of $FeCl_2.4H_2O$ in a N_2 environment that was stirred for 1 ½ hours while at 115°C to degas the mixture. The iron precursor was then heated to 230°C; after this temperature has been achieved the sulfur precursor was then injected into the

iron precursor where it maintained this temperature while being stirred for 2 hours. After the allotted 2 hours had passed, the mixture was cooled to 85°C when upon reaching this temperature a few drops of chloroform were added to prevent coagulation. To clean this mixture it was then washed with methanol three times in a centrifuge at 5000 RPMs for 10 minutes.

The previously mentioned setup for the experiment has been outlined in Table 2.1 with an emphasis on the main changes between each stage of the experiment. Column 1 of the table outlines the ingredients used for the sulfur precursor while column 2 outlines the ingredients used for the iron precursor. The final column displays the temperature of the iron precursor before the inclusion of the sulfur precursor, as well as the temperature that is maintained during the nucleation process.

2.2 Sample Preparation for Characterization

To prepare the nanocrystals for characterization there were two basic methodologies, the first one was to use the as-synthesized material, while the other was to dilute the material in a solvent. The as-synthesized preparation was done for the techniques XRD, SEM, and TEM and was completed by simply putting an appropriate amount of the sample onto a sample holder in such a way that the techniques could work in optimal conditions. Due to the fact that the material is a semiconductor there were no other special procedures necessary for SEM or TEM. Dilution of the material in a solvent was done for micro-Raman and UV-Vis-NIR spectroscopy. This was carried out by combining the material and a solvent, usually chloroform, and using a sonicator for 1 hour to ensure that the material and the solvent were completely combined. This solution was then either spin-coated onto a slide or used in a <COVET> to hold the solution for measurement.

3. Results and Discussion

The experiment can basically be divided into four main stages, the first stage is the synthesis of iron pyrite nanocrystals with the sulfur precursor is 500 mg of sulfur and 15 mL of diphenyl ether while the iron precursor consist of 10 mL of octylamine and 2.5 mmol of $FeCl_2.4H_2O$ and having the main variable being the variance of the synthetic temperature. After the first stage the synthetic temperature of 230°C was chosen for each of the following three stages due to the results in the first stage. The second stage saw the inclusion of 2.0 mmol of TOPO in the iron precursor, while the sulfur precursor replaced the diphenyl ether with octylamine. For the third stage the sulfur precursor remained steady while the iron precursor no longer included the surfactant TOPO. The fourth and final stage saw the replacement of octylamine for oleylamine in both the sulfur and iron precursor.

3.1 Stage One

In the first stage of the experiment the sulfur precursor is made of 500 mg of sulfur and 15 mL of diphenyl ether while the iron precursor consist of 10 mL of octylamine and 2.5 mmol of $FeCl_2.4H_2O$. This stage dealt with the effect of the change of the synthetic temperature for the nanocrystals and that effect as how it relates to the XRD spectrum and the UV-Vis-NIR absorption spectrum.

The UV-Vis-NIR spectrum for the iron pyrite nanocrystals with the synthetic temperature of 175°C, 215°C, and 260°C are shown in Fig. 3.1. The effect of the synthetic temperature is easily discernible on the sample where the temperature reached 260°C due to the absorption

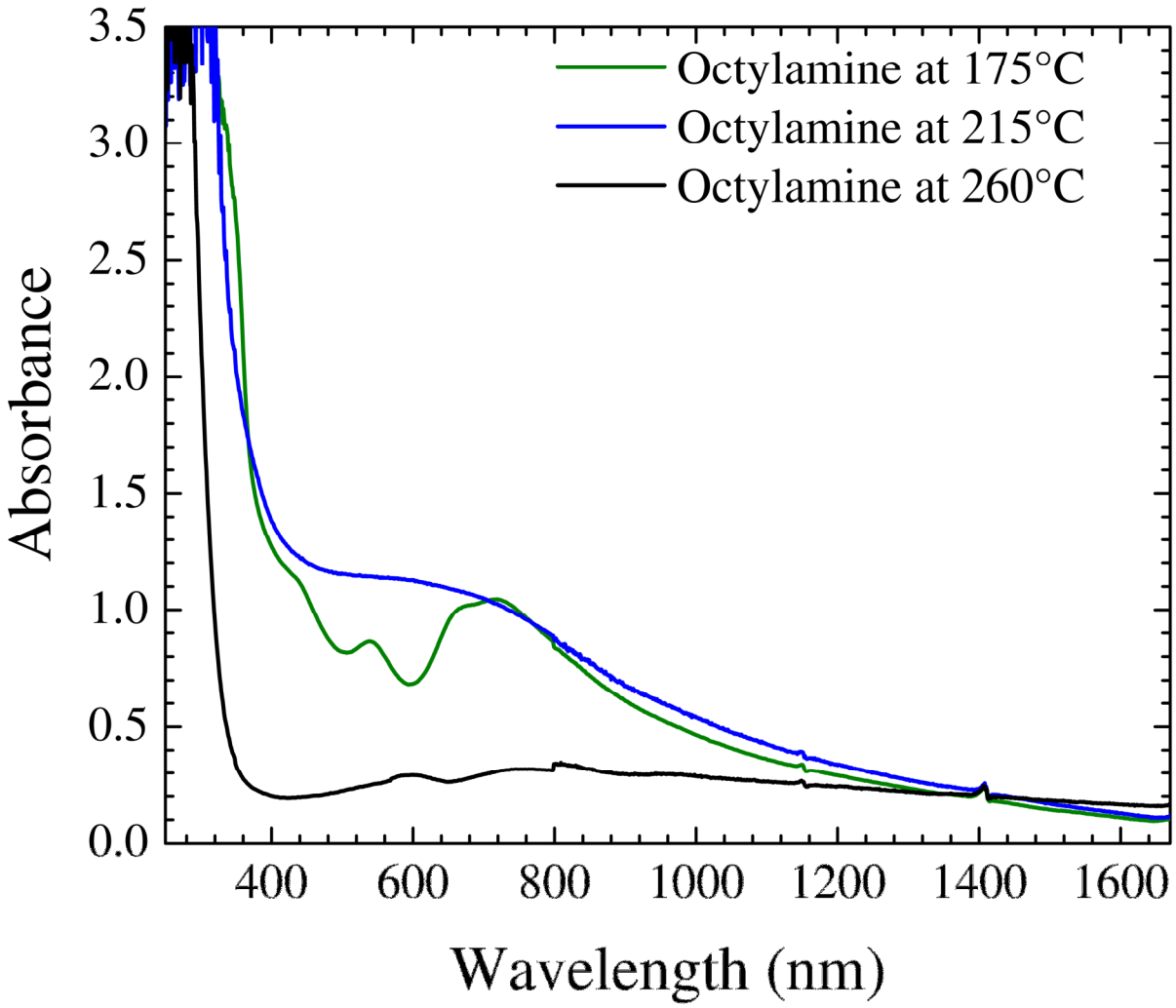

Fig. 3.1. The absorption spectra of iron pyrite nanocrystals with a varied synthetic temperature of 175°C, 215°C, and 260°C to examine the difference in absorption of the various nanocrystals.

spectrum of the iron pyrite drastically reduced compared to the other two spectra. For the samples where the temperature was 175°C and 215°C the absorption spectra exhibited considerable absorption in the visible light spectrum for both the 175°C and 215°. The spectrum for the 215°C exhibited a greater amount of absorption for the range of 400 to 700 nm due to the dip in absorption in that range by the 175°C sample. Considering the solar spectrum there is a need to optimize the absorption in that particular wavelength range [25].

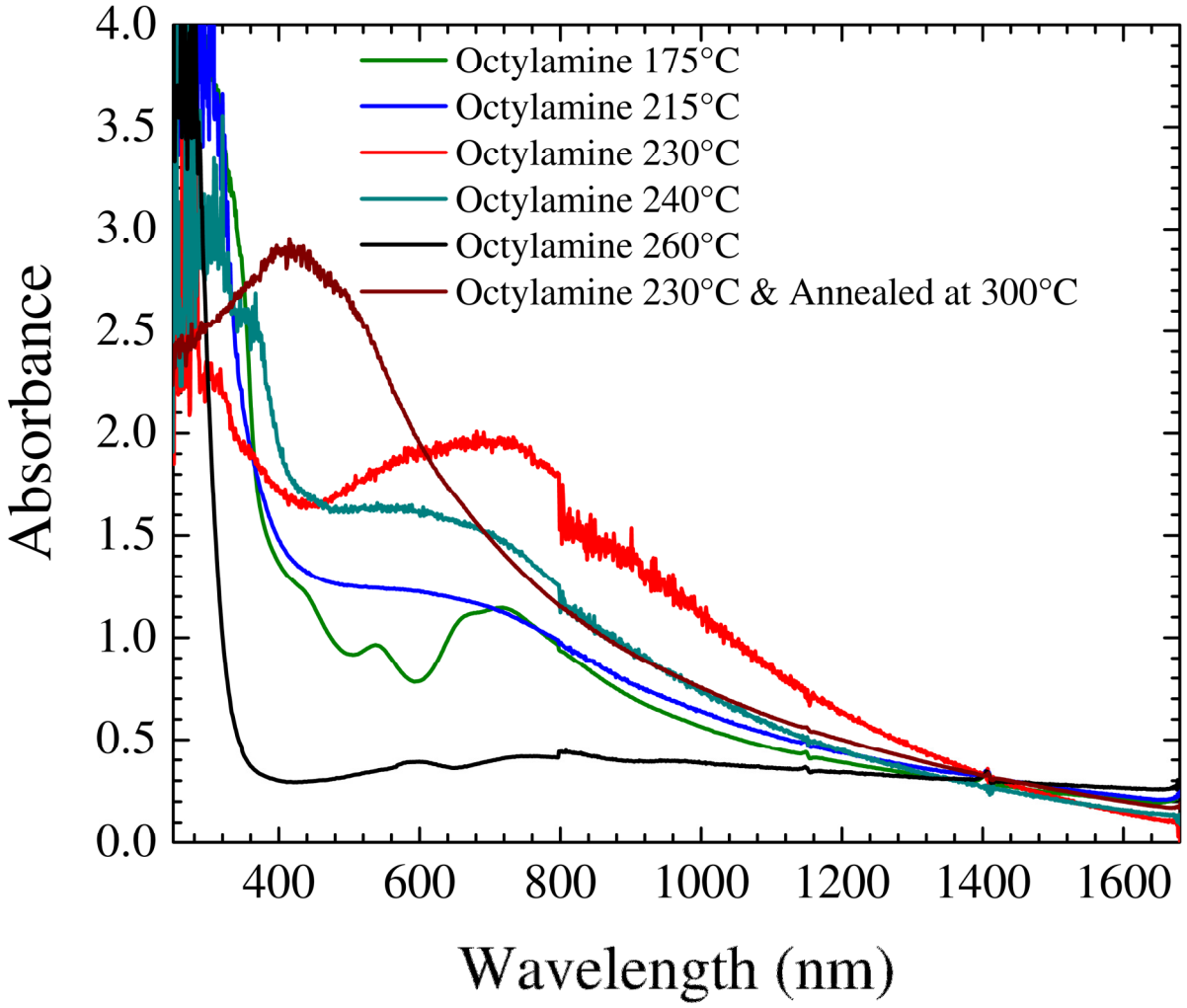

Fig. 3.2. The absorption spectra of iron pyrite nanocrystals with a varied synthetic temperature from 175°C to 260°C to compare the various iron pyrite nanocrystals absorption.

Further experimentation revealed that the optimum UV-Vis-NIR absorption of the nanocrystals synthetic temperature was greater 215°C previously shown. The UV-Vis-NIR absorption spectra in Fig. 3.2 displays an increase in the overall absorption for the 230°C sample when compared to the 215°C sample. As the synthetic temperature increased beyond 230°C for the iron pyrite nanocrystals the absorption decreased for both the 240°C and the 260°C samples. As previously shown in Fig. 3.1, the absorption spectrum of the synthetic temperature of the iron

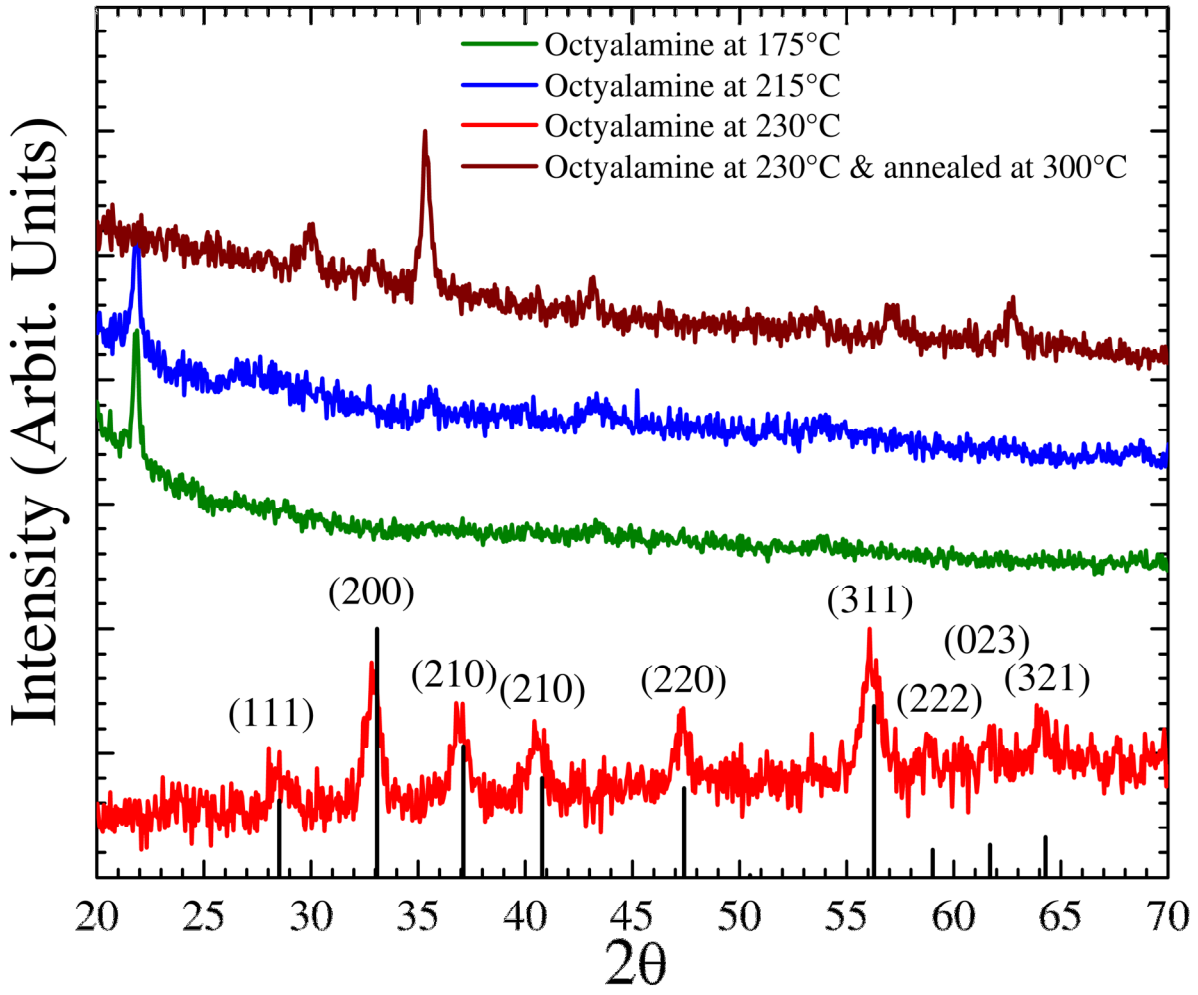

Fig. 3.3. The XRD of iron pyrite nanocrystals with a varied synthetic temperature from 175°C to 260°C to compare the various iron pyrite nanocrystals. Only the sample at the synthetic temperature of 230°C matches the referenced pattern shown by the vertical lines.

pyrite nanocrystals at 260°C exhibited considerably less absorption than any of the other synthetic conditions. The absorption spectrum of the 240°C sample exhibited a stronger absorption than the 215°C sample but less than the 230°C. Considering the absorption spectrum of the 230°C sample, the sample was then annealed at 300°C with the effect on the absorption was mixed. Shown in Fig. 3.2 is difference in the absorption between the annealed and non-annealed samples that held the synthetic temperature of 230°C. For the range of 350 to 600 nm

the absorption of the annealed sample was greater than the non-annealed sample, however, at wavelengths greater than 600 nm the non-annealed sample exhibited greater absorption.

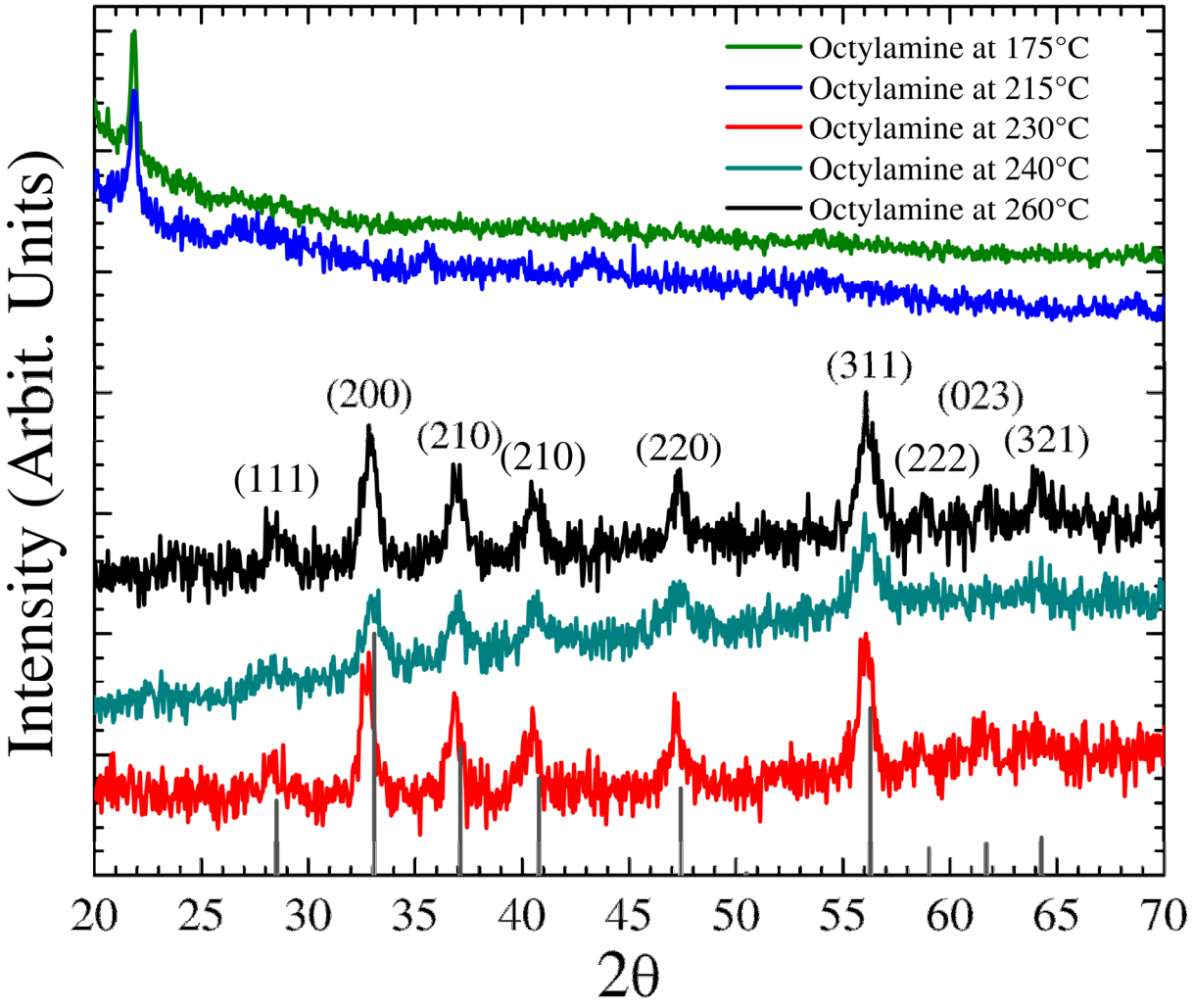

Fig. 3.4. The XRD of iron pyrite nanocrystals with a varied synthetic temperature from 175°C to 260°C to compare the various iron pyrite nanocrystals. Only the samples at the synthetic temperature of 230°C, 240°C, and 260°C matches the referenced pattern shown by the vertical lines.

The next step required the investigation of the XRD spectrum for the various samples to determine if the material exhibited peaks indicative of phase-pure face-centered cubic iron pyrite nanocrystals. The XRD spectrum of both the 175°C and the 215° samples showed no

identifiable peaks of iron pyrite nanocrystals or any major peaks for that matter in Fig. 3.3. While the 230°C sample annealed at 300°C did show some major peaks, there were not enough peaks, both major and minor, to readily identify the sample as iron pyrite. The 230°C sample showed both major and minor peaks that exhibited face-centered cubic iron pyrite and is able to be indexed as such at 28.2°, 33.8°, 36.9°, 40.5°, 47.3°, 56.28°, 59.02°, 61.70°, and 64.28° to the following corresponding crystal phases of (111), (200), (210), (211), (220), (311), (222), (023), and (321), respectively. To ascertain which temperature is the optimal synthetic temperature, the remaining samples were also measured using the XRD with the spectra for those samples shown in Fig. 3.4. The two samples previously mentioned, 175°C and 215°C, did not show any peaks indicative of iron pyrite, while the other three samples, 230°C, 240°C, and 260°C, showed excellent peaks that exhibit face-centered cubic iron pyrite characteristics with all the indexed angles previously mentioned. By applying Bragg's law to the three samples at the angle of 33.8° it is calculated that the lattice spacing is 0.27 nm for the each synthetic temperatures of 230°C, 240°C, and 260°C, which is in agreement with Wang et al. [18]. This consistency in the lattice spacing helps to illustrate the precision at which the synthesis method has achieved, despite a change in the synthetic temperature from 230°C to 260°C. The main attribute that is apparent from the XRD that differs slightly between the three samples is the difference in grain size calculated by the Scherrer formula. The synthetic temperature of 230°C was calculated to have a grain size of 8.9 nm, while both the 240°C and the 260°C samples were calculated to have a slightly larger grain size of 9.7 nm.

The SEM images in Fig. 3.5 and Fig. 3.6 show the particle structure of the iron pyrite with different synthetic temperatures. For the sample with the synthetic temperature of 230°C

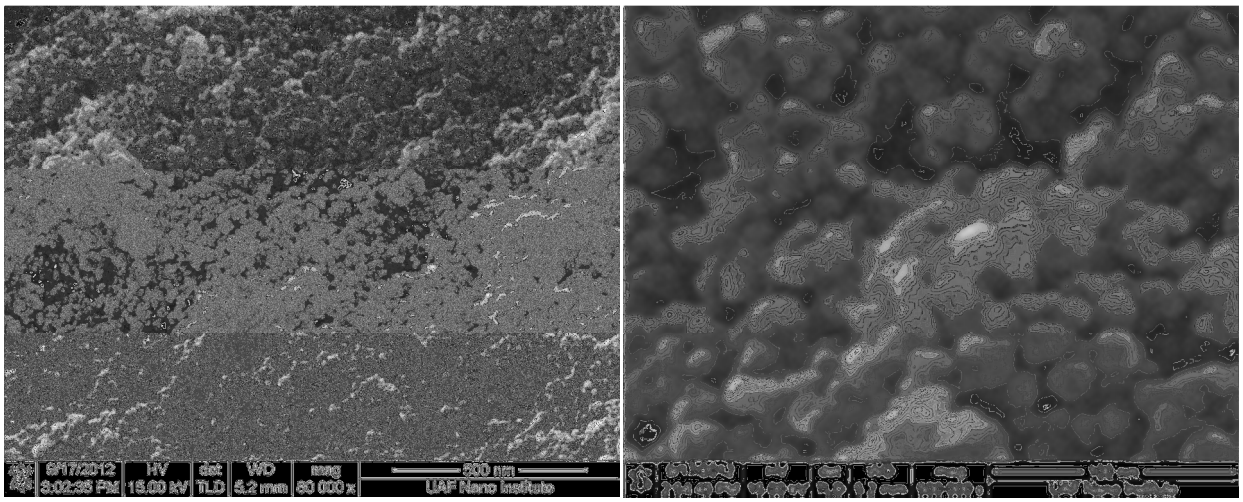

(a) (b)

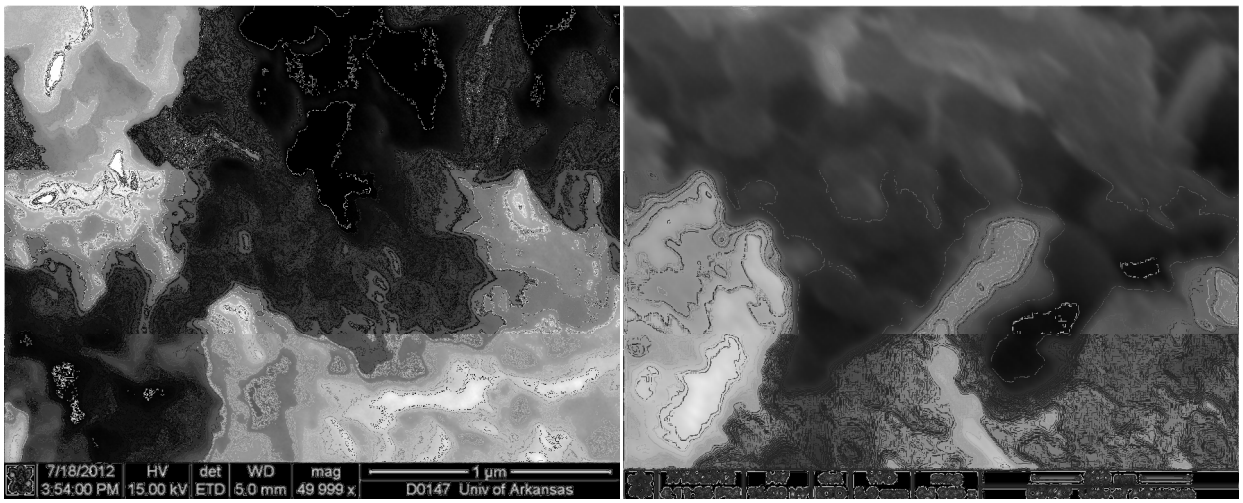

(c) (d)

Fig. 3.5. All of the above samples are the SEM image of iron pyrite at the synthetic temperature of 230°C. For the images in (c) and (d) the iron pyrite is also annealed at 300°C.

shown in Fig. 3.5 (a) and (b) there is an apparent structure for the particles with the average particle size is shown to be 30 nm. At this level of magnification it is impossible to discern what the crystal structure of the iron pyrite is. After annealing the 230°C sample at 300°C the iron pyrite no longer exhibited any uniform structure with every particle exhibiting a different shape and there was not a uniform size between the particles either. The iron pyrite shown in Fig. 3.6

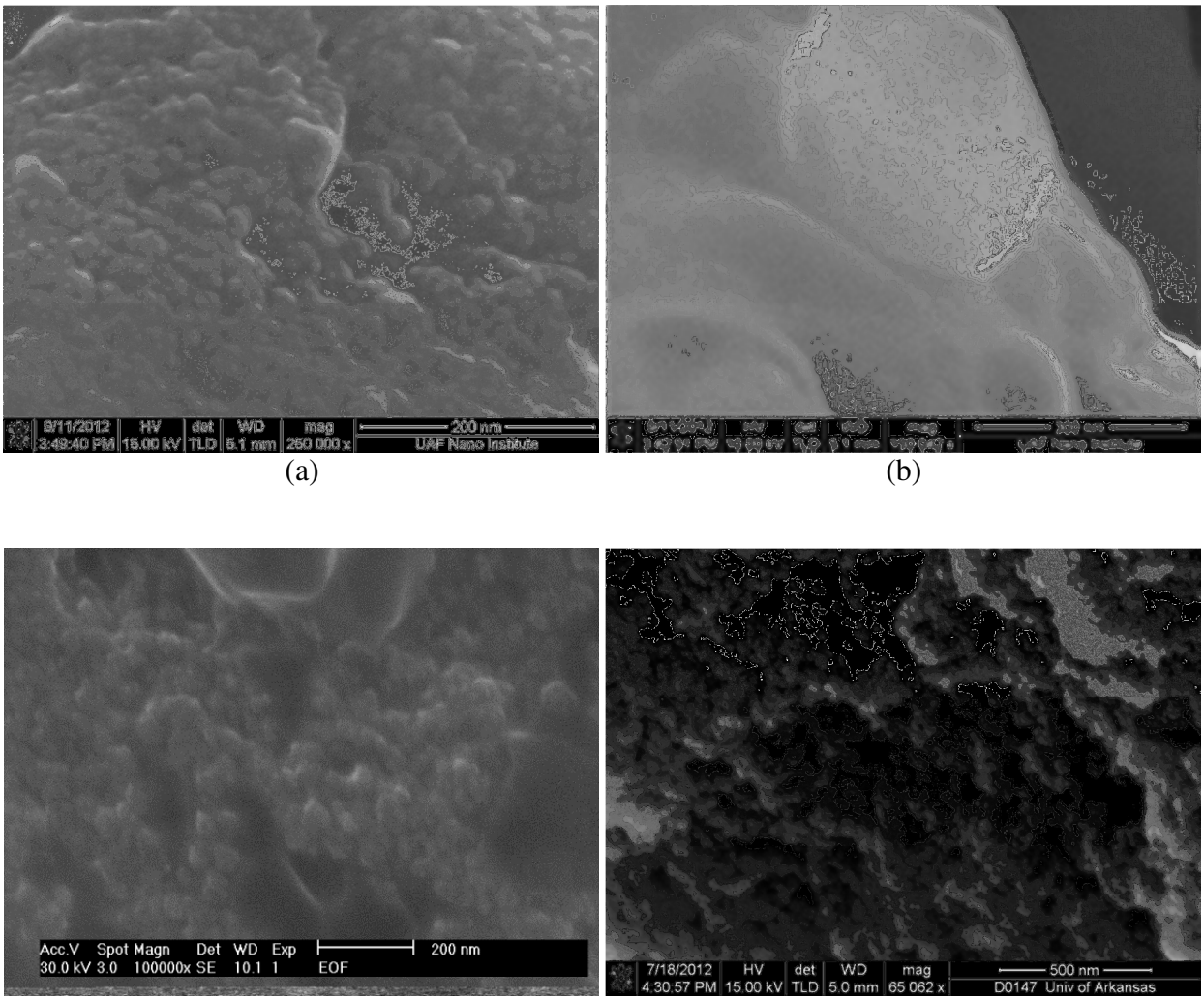

(a) (b)

(c) (d)

Fig. 3.6. The SEM images of the as-synthesized iron pyrite nanocrystals at various synthetic temperatures, (a) and (b) are at 215°C, while (c) is at 245°C, and (d) is at 260°C.

(a) and (b) shows the slight formation of structured particles with the size ranging from 30 nm all the way to 150 nm. After increasing the synthetic temperature to 245°C the previously shown structure of the iron pyrite in Fig. 3.5 (a) and (b) is whittled down to glimpses of both the previous structure and the appearance of larger non-uniform particles shown in Fig. 3.6 (c). When the synthetic temperature is increased to 260°C there appears to be decent structure from

the iron pyrite nanocrystals with the average particle size ranging from 30 to 50 nm. After examining the results from the XRD, UV-Vis-NIR absorption, and the SEM images from the previously described samples the synthetic temperature of 230°C was chosen due to the absorption shown, the uniformed particle structure, and the XRD spectrum. The experimentation with annealing resulted in a severe detriment for the XRD spectrum and the SEM images.

While the synthetic temperature of both 240°C and 260°C showed the face-centered cubic iron pyrite according to the XRD spectrum, because the 260°C showed considerably less absorption that temperature was not considered. The 240°C temperature showed decent particle structure, but the absorption, while acceptable, was not on par with the absorption of the 230°C sample. Considering the weight of the decision fell more towards the XRD spectrum and the absorption spectrum the choice for 230°C synthetic temperature was fairly obvious after combining the two main factors, especially once the SEM images included in the decision.

3.2 Stage Two

Based on the synthetic temperature 230°C, this stage and the following stage experimented with the effect of using the same amine for both the iron and sulfur precursor as well as how the addition or absence of TOPO could affect the properties of the iron pyrite nanocrystals. One of the main reasons to include TOPO is because of the usage of TOPO as a stabilizing agent that has been reported to passivate both iron and sulfur atoms thereby decreasing surface decomposition [13]. With the decrease in the surface decomposition the longevity of the appropriate properties for photovoltaic devices is increased.

The iron pyrite nanocrystals with TOPO with a synthetic temperature of 230°C have been compared to the previous iron pyrite nanocrystals synthesized with octylamine and dipenhyl

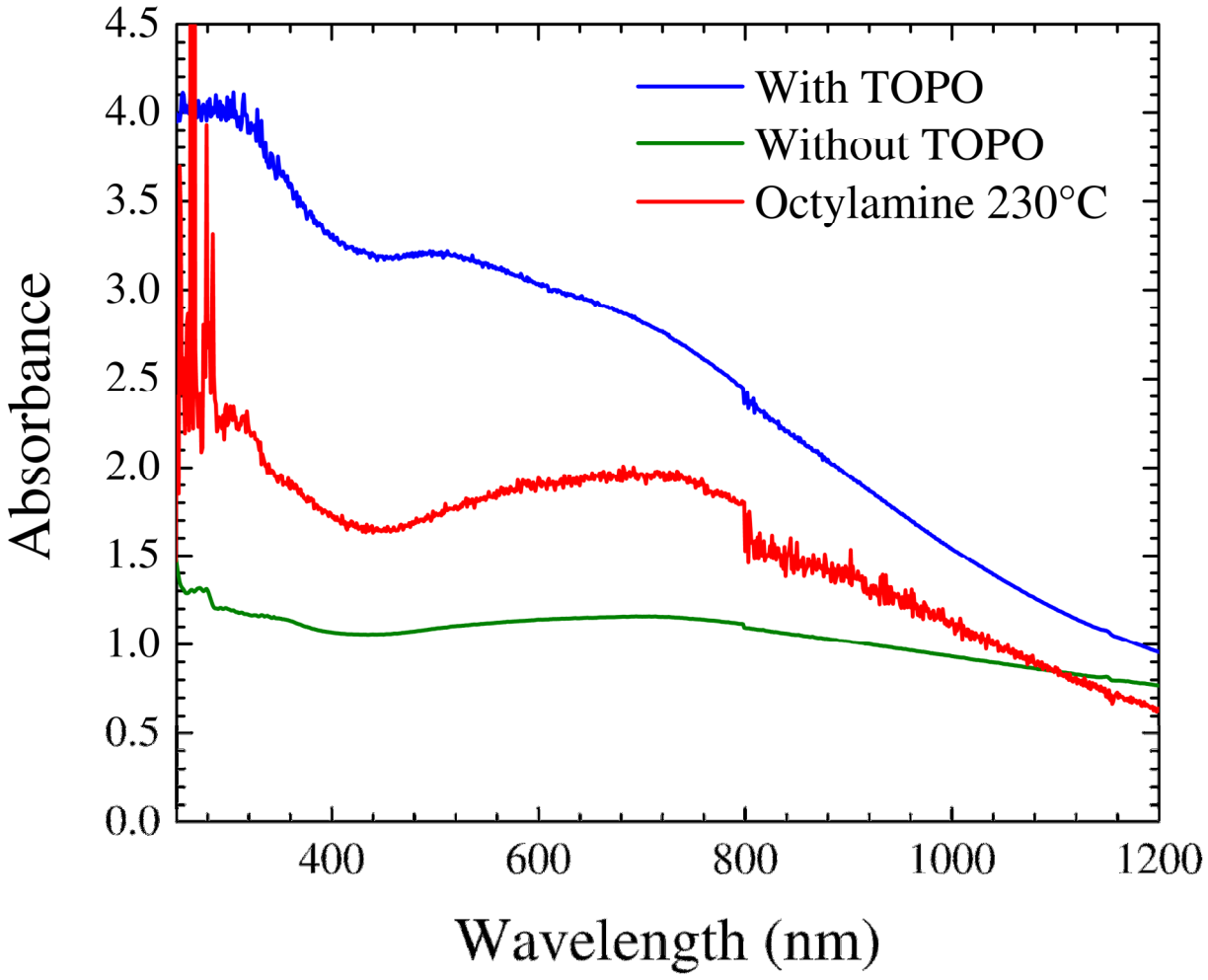

Fig. 3.7. The absorption spectra of iron pyrite nanocrystals where one sample is synthesized with TOPO, one is synthesized without TOPO, and the previous sample octylamine at the synthetic temperature of 230°C. The top line is the iron pyrite nanocrystals with TOPO, the middle line is the octylamine at 230°C, and the bottom line is the iron pyrite nanocrystals without TOPO.

ether with a synthetic temperature of 230°C. In Fig. 3.7 the UV-Vis-NIR spectrum for three different iron pyrite nanocrystal samples are shown. The blue line, referred to as with TOPO in the legend, is the sample made with octylamine for both the iron and sulfur precursor with the inclusion of the surfactant TOPO. The green line, referred to as without TOPO is another sample made with octylamine for both the iron and sulfur precursor, however, it does not include TOPO.

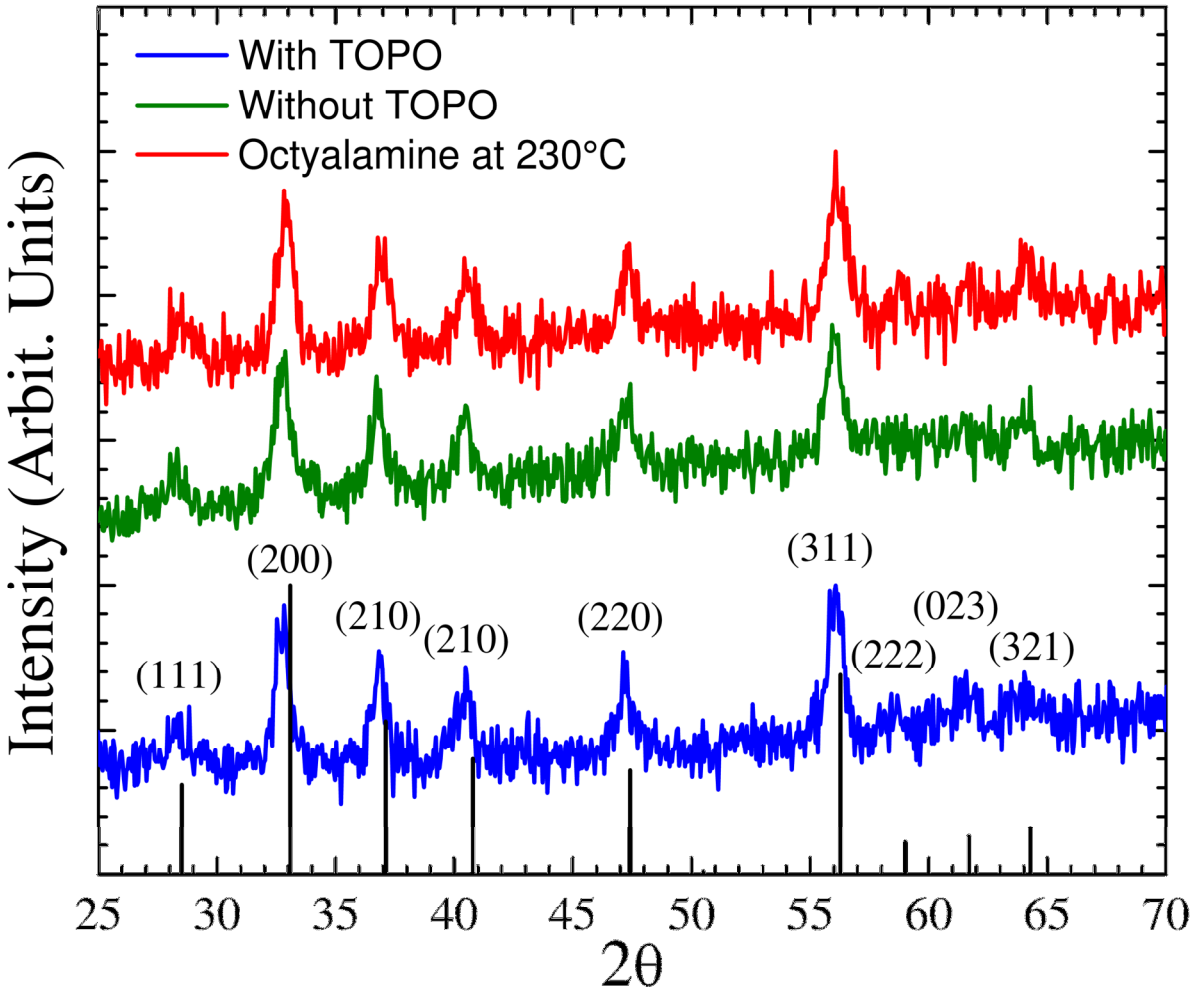

Fig. 3.8. The XRD spectra of iron pyrite nanocrystals where one sample is synthesized with TOPO, one is synthesized without TOPO, and the previous sample octylamine at the synthetic temperature of 230°C. All three patterns match the vertical lines of the reference pattern.

For the red line, referred to as Octylamine at 230°C, is the sample discussed in stage one, made from dipenhyl ether in the sulfur precursor and octylamine in the iron precursor with a synthetic temperature of 230°C. When comparing the sample with TOPO to the Octylamine at 230°C sample there is an obvious increase in the absorption throughout the spectrum, with a particular increase in the absorption of the sample with TOPO in the range from 300 to 800 nm. Another

major difference between the absorption spectra is the less pronounced dip in absorption around 400 nm for the sample with TOPO, and thus leading to an even greater difference in the absorption for that sample.

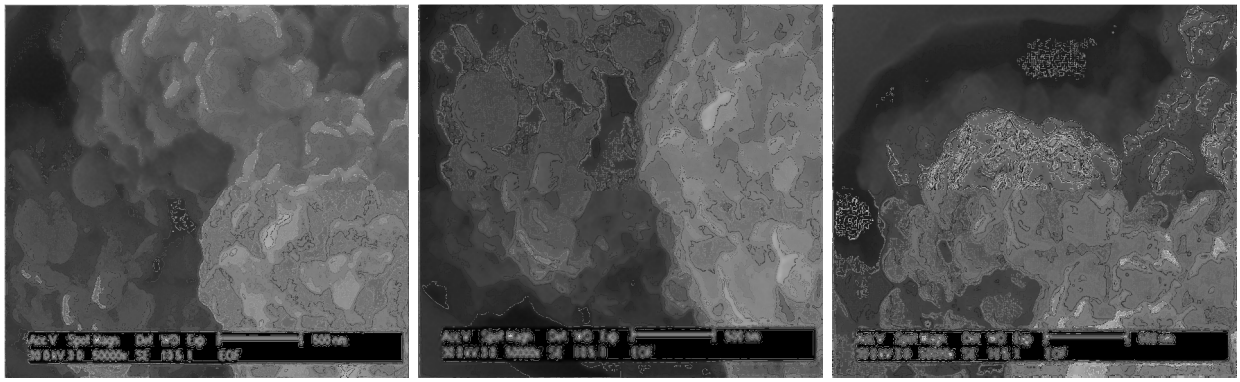

(a) (b) (c)

Fig. 3.9. The SEM images of as-synthesized iron pyrite nanocrystals containing the surfactant TOPO are shown in (a), (b), and (c) all with a linear scale of 500 nm.

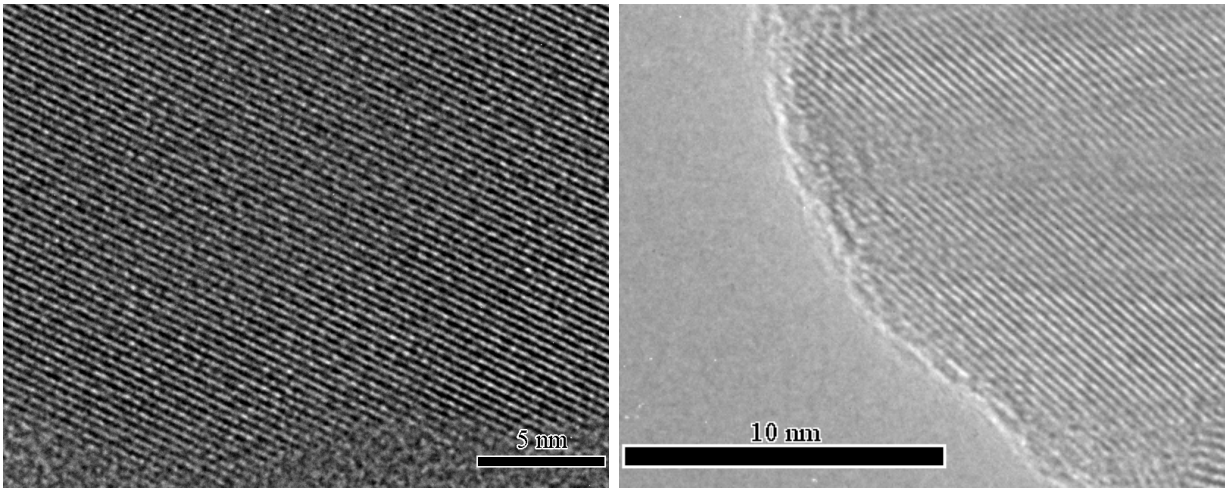

(a) (b)

Fig. 3.10. The TEM images for the iron pyrite nanocrystals for the sample of nanocrystals with TOPO is shown in (a), while (b) contains the TEM image of the nanocrystals without TOPO.

In Fig. 3.8 the legend and corresponding line colors to samples remains the same as it was described for Fig. 3.7. The XRD spectrum for both the sample with TOPO and the octylamine at

230°C sample both exhibited face-centered cubic iron pyrite that were indexed at 28.2°, 33.8°, 36.9°, 40.5°, 47.3°, 56.28°, 59.02°, 61.70°, and 64.28° to the following corresponding crystal phases of (111), (200), (210), (211), (220), (311), (222), (023), and (321), respectively. A reference pattern (ICDD number 00-042-1340) was used to confirm the phase-pure face-centered cubic nature of the iron pyrite nanocrystals and is represented in the Fig. 3.8 by the black vertical lines. There was also no appreciable difference between the two samples for the XRD spectra, including the lattice spacing that was calculated to be 0.27 nm, the same as it was calculated before. The synthetic conditions used imposed a slight shift on all the peaks for each sample of iron pyrite nanocrystals.

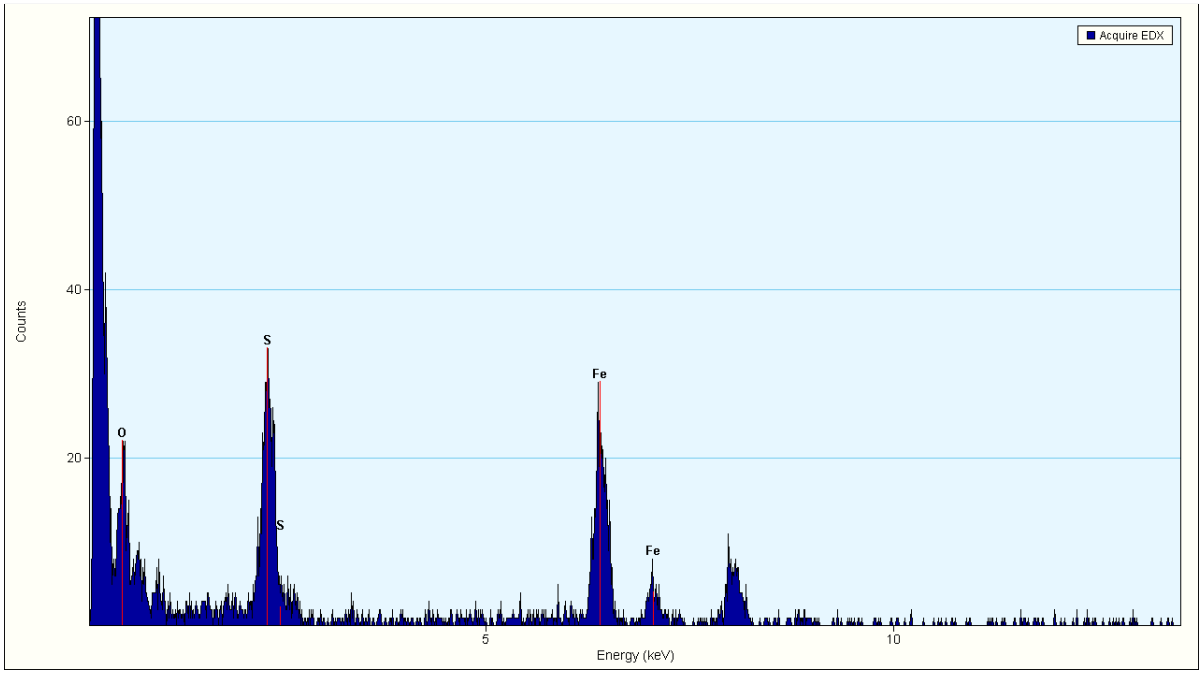

Fig. 3.11. The EDX of the iron pyrite nanocrystals with TOPO that shows the presence of iron (Fe) and sulfur (S).

The SEM image in Fig. 3.9 (a), (b), and (c) shows the phase-pure face-centered cubic iron pyrite nanocrystals with TOPO that exhibits particle sizes that range from 70 to 250 nm. Despite

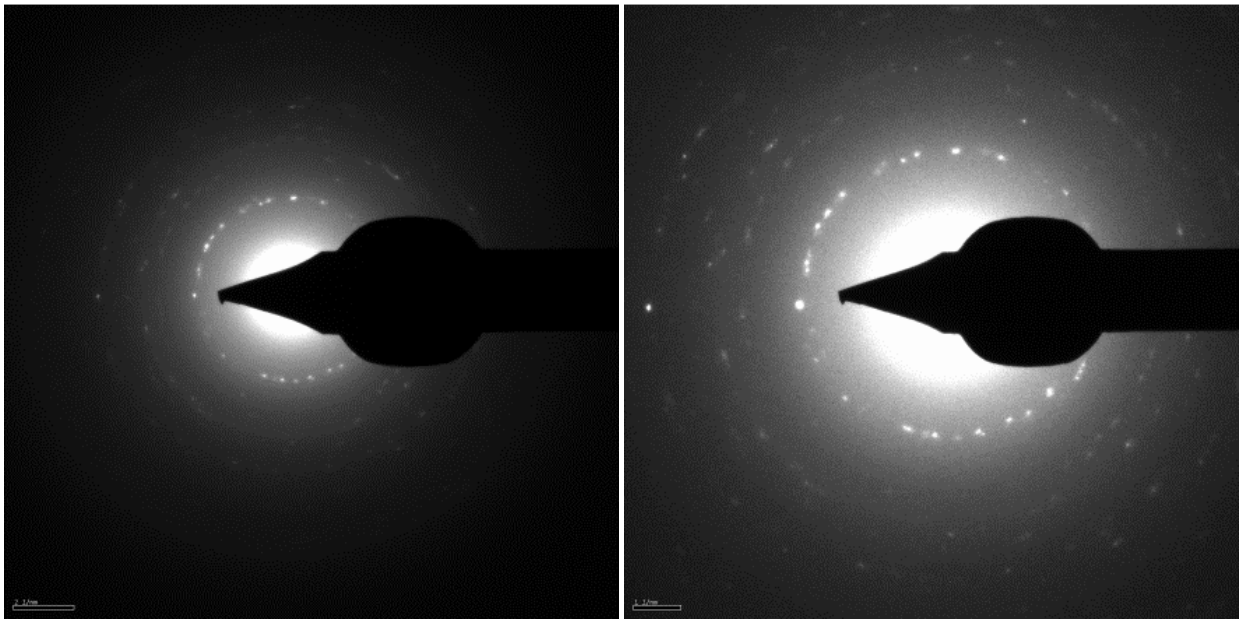

(a) (b)

Fig. 3.12. The crystalline diffraction pattern of the iron pyrite nanocrystals with TOPO obtained from the TEM.

having been measured from the XRD in Fig. 3.8 as face-centered cubic crystalline structure, at the particle level there is not an apparent ordered structure for the SEM images in Fig. 3.9. To investigate the lattice spacing and grain size of the iron pyrite nanocrystals with TOPO it is necessary to look into the TEM images shown in Fig. 3.10 (a) and (b). According to the TEM image in Fig. 3.10 (a) the grain size is 17.3 nm while exhibiting a lattice spacing of 0.27 nm for the iron pyrite nanocrystals with TOPO with this lattice spacing being confirmed with Wang et al. [18]. The grain size is in slight discrepancy to the calculated grain size of 13.4 nm by the Scherrer formula at 33.8°, but this slight discrepancy can be accounted for due to the agglomerated grains that can increase the difficulty of precise and consistent grain size results. The aforementioned lattice spacing of 0.27 nm shown in the TEM image is further confirmed by the same lattice spacing of 0.27 nm that was calculated using the XRD and Bragg's law at 33.8° in Fig. 3.8.

Using the EDX in Fig. 3.11 it is easily discernible that there is a presence of iron and sulfur, as well as oxygen. Due to the nature of this particular EDX testing procedures, oxygen will always be present due to a lack of stringent enough controls on both the testing environment as well as sample handling to completely prevent oxygen from appearing in the EDX test results. Furthering the strong crystal structure of the face-centered cubic iron pyrite nanocrystals with TOPO shown by the XRD in Fig. 3.8, is the TEM image in Fig. 3.12 that shows three rings in Fig. 3.12 (a) and four rings in Fig. 3.12 (b). The number of rings corresponds to the strength of the crystal structure in that particular part of iron pyrite nanocrystals with TOPO.

3.3 Stage Three

After the examination on the iron pyrite nanocrystals synthesized with TOPO the next step is to remove the TOPO to attempt to synthesize the iron pyrite nanocrystals with a single amine to act as both a surfactant and a solvent for the precursors, without the aid of TOPO. This is done to try and increase the possible optical properties of the iron pyrite nanocrystals.

The measurement of the UV-Vis-NIR spectrum for the iron pyrite nanocrystals synthesized with octylamine for both the sulfur and iron precursor without the use of TOPO is shown in Fig. 3.7 where it is compared to both the sample prepared with TOPO as well as the previously mention sample with the synthetic temperature of 230°C. The blue line, referred to as with TOPO in the legend, while the green line is referred to as without TOPO. For the red line, referred to as Octylamine at 230°C, is the sample discussed in stage one, made from dipenhyl ether in the sulfur precursor and octylamine in the iron precursor with a synthetic temperature of 230°C. The sample with TOPO is shown to exhibit more absorption around 1200 nm that then Octylamine at 230°C sample. At less than 1100 nm the sample without TOPO shows less

absorption than either than sample with TOPO or the Octylamine at 230°C sample, particularly in the visible light spectrum where both the with TOPO and the Octylamine at 230°C exhibit an increase in absorption, particularly compared to the sample without TOPO.

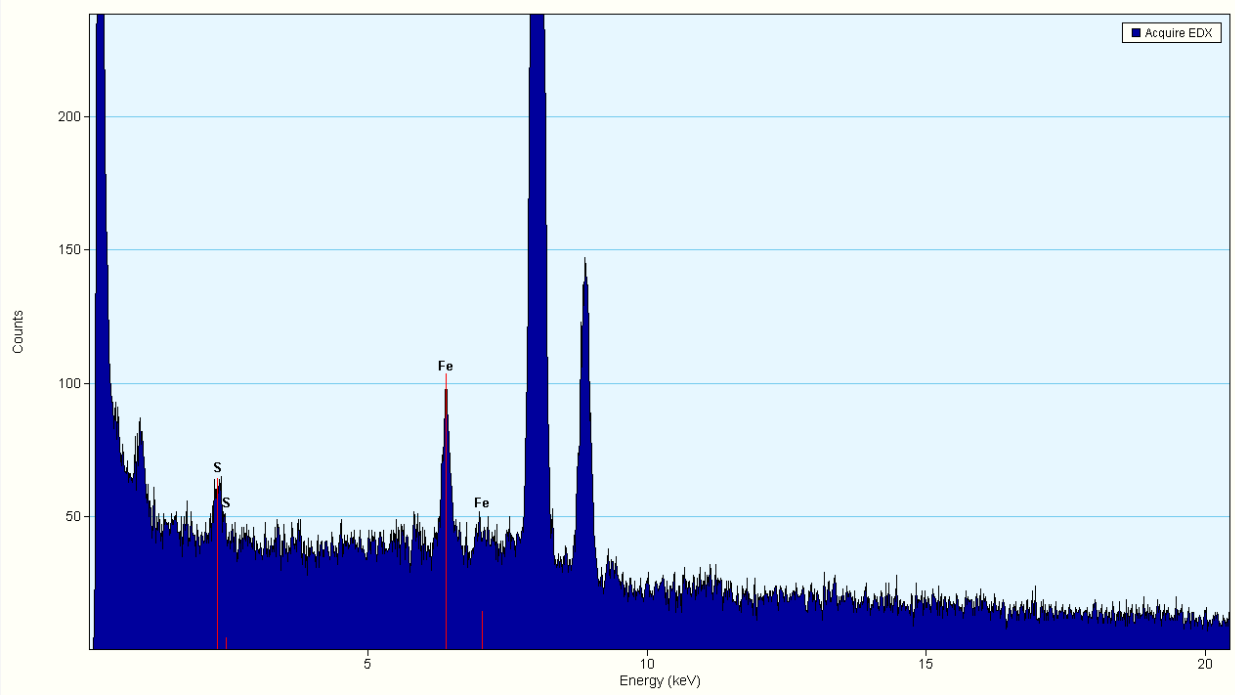

Fig. 3.13. The EDX of the iron pyrite nanocrystals without TOPO that shows the presence of iron (Fe) and sulfur (S).

For the XRD spectrum in Fig. 3.8 the legend and corresponding line colors are the same as it was described for Fig. 3.7. The XRD spectra for the three samples were compared to the reference pattern from ICDD that numbered 00-042-1340. While the XRD spectrum for the with TOPO and the Octylamine at 230°C sample both exhibited the face-centered cubic iron pyrite that was properly indexed as previously mentioned, the sample without TOPO showed the following indexes at 28.2°, 33.8°, 36.9°, 40.5°, 47.3°, 56.28°, and 64.28° to the following corresponding crystal phases of (111), (200), (210), (211), (220), (311), and (321) due to a lack of easily identifiable peaks at 59.02° and 61.70°. Considering the weakness of the peaks at

59.02° and 61.70° from the reference pattern from ICDD it is easily discernible that iron pyrite nanocrystals that exhibit slightly weaker peaks throughout would not exhibit the peaks at 59.02° and 61.70° first. Using the EDX in Fig. 3.13 it is apparent that there is a presence of iron and sulfur in the iron pyrite without TOPO. There is also a fairly large amount of other materials, excluding oxygen, that were not as easily apparent in the iron pyrite with TOPO sample in Fig. 3.11.

3.4 Stage Four

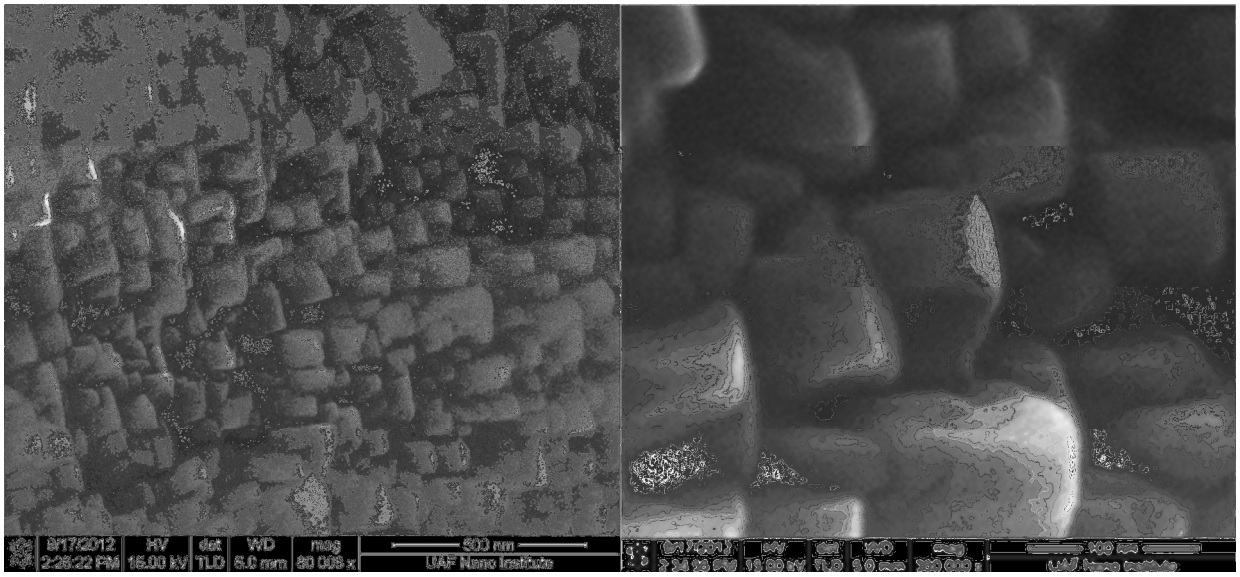

(a) (b)

Fig. 3.14. The SEM images of as-synthesized iron pyrite nanocrystals with oleylamine is shown in (a) and (b) where (a) has a linear scale of 500 nm while (b) has a linear scale of 100 nm.

After the detriment of properties for the previous sample made with octylamine for both the iron and sulfur precursor without the aid of TOPO, particularly with relation to the XRD pattern shown in Fig. 3.8 where the peaks at 59.02° and 61.70° was not as apparent as it was for the sample made with TOPO. This has led to using oleylamine rather than octylamine for both the iron and sulfur for the purpose of having a singular amine for the sulfur and iron precursors.

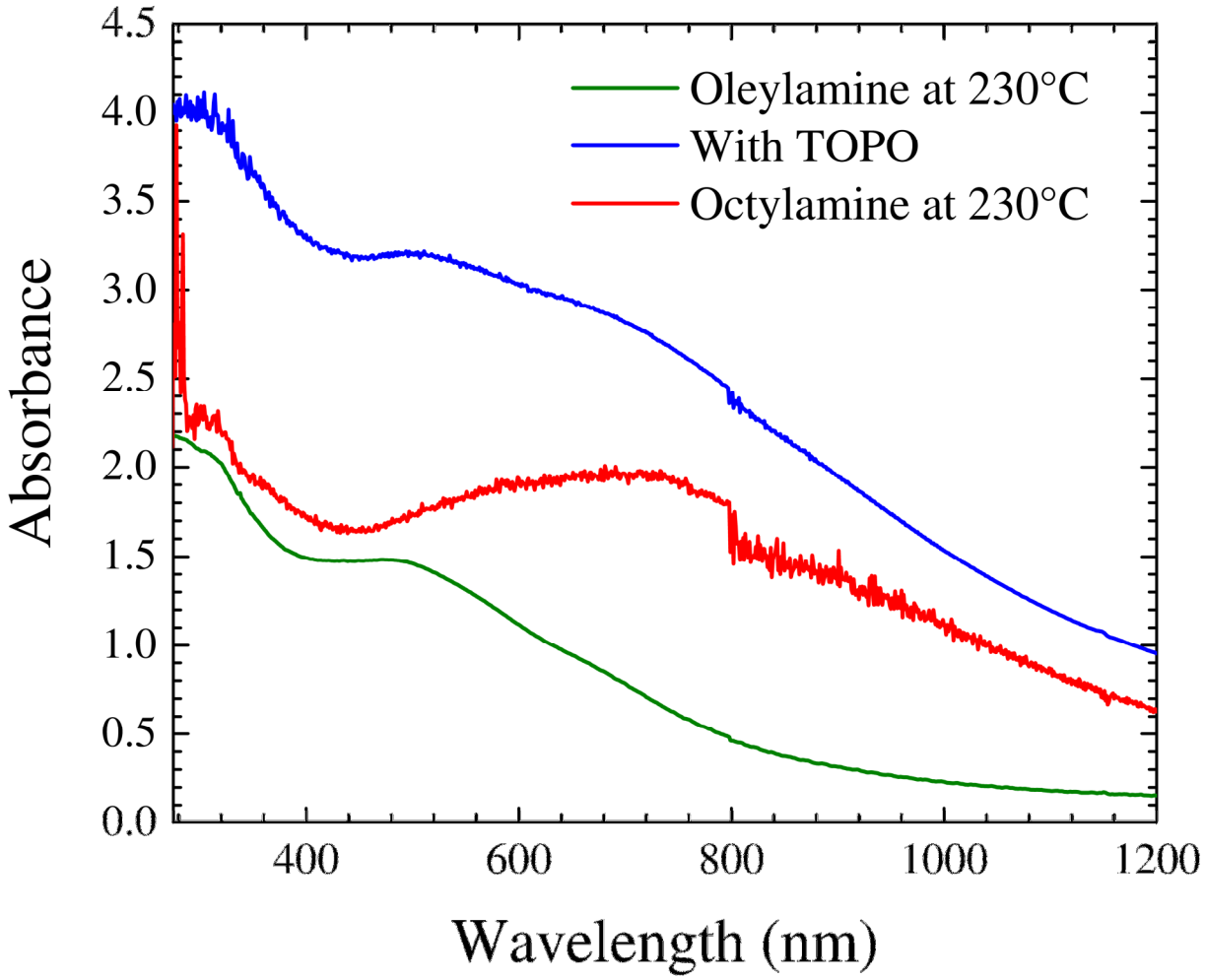

Fig. 3.15. The UV-Vis-NIR absorption spectra of iron pyrite nanocrystals with TOPO, octylamine at the synthetic temperature of 230°C, and the oleylamine sample with the top line being the sample with TOPO, the middle line is the octylamine, and the bottom line is the Oleylamine.

The SEM image for the iron pyrite nanocrystals with oleylamine for both the sulfur and iron precursors is shown in Fig. 3.14. This figure displays the particle size for the iron pyrite nanocrystals to range from 50 to 100 nm while displaying a cubic structure for the particles. The particles for an organized pattern due to the structure of each particle allowing for a somewhat ordered. The SEM images for the iron pyrite nanocrystals with oleylamine are a vast

improvement over the SEM images in Fig. 3.5, Fig. 3.6, and Fig. 3.9 for the previously mentioned iron pyrite nanocrystals. The improvement of the SEM images for the iron pyrite nanocrystals with oleylamine is for both the structure of the particles, as well as the range in size being considerably more consistent throughout.

The absorption of the iron pyrite nanocrystals shown in Fig. 3.15 displays a smoother absorption curve of the oleylamine as compared to the octylamine at 230°C and the iron pyrite nanocrystals with TOPO. For the sample with the octylamine at 230°C there is noise in the absorption shown in the wavelength range of 800 to 1000 nm, and during the range of 400 to 700 nm the absorption in the octylamine sample decreases in absorption as the wavelength decreases, while the oleylamine sample is increasing the absorption in the same range. When compared to the octylamine at 230°C the oleylamine behaves generally the same, save for as the sample approaches 300 nm the octylamine at 230°C shows some noise in the absorption while the oleylamine does not. Based on Kubelka-Munk equation and the absorption spectrum in Fig. 3.15 the direct band gap can be extrapolated to be approximately 1.35 to 1.4 eV.

The XRD for the iron pyrite nanocrystals synthesized with oleylamine is again compared with the previously mentioned iron pyrite nanocrystals with TOPO as well as the iron pyrite nanocrystals synthesized with octylamine at 230°C, respectively the blue, green, and red lines. As previously mentioned for Fig. 3.3, Fig. 3.4, and Fig. 3.8, the synthetic conditions upon the synthesis of the iron pyrite nanocrystals produced a slight shift compared to the reference pattern (ICDD number 00-042-1340) that is represented by a vertical black line in Fig. 3.16. The oleylamine sample in Fig. 3.16 is indexed at 28.2°, 33.8°, 36.9°, 40.5°, 47.3°, 56.28°, 59.02°, 61.70°, and 64.28° to the following corresponding crystal phases of (111), (200), (210), (211),

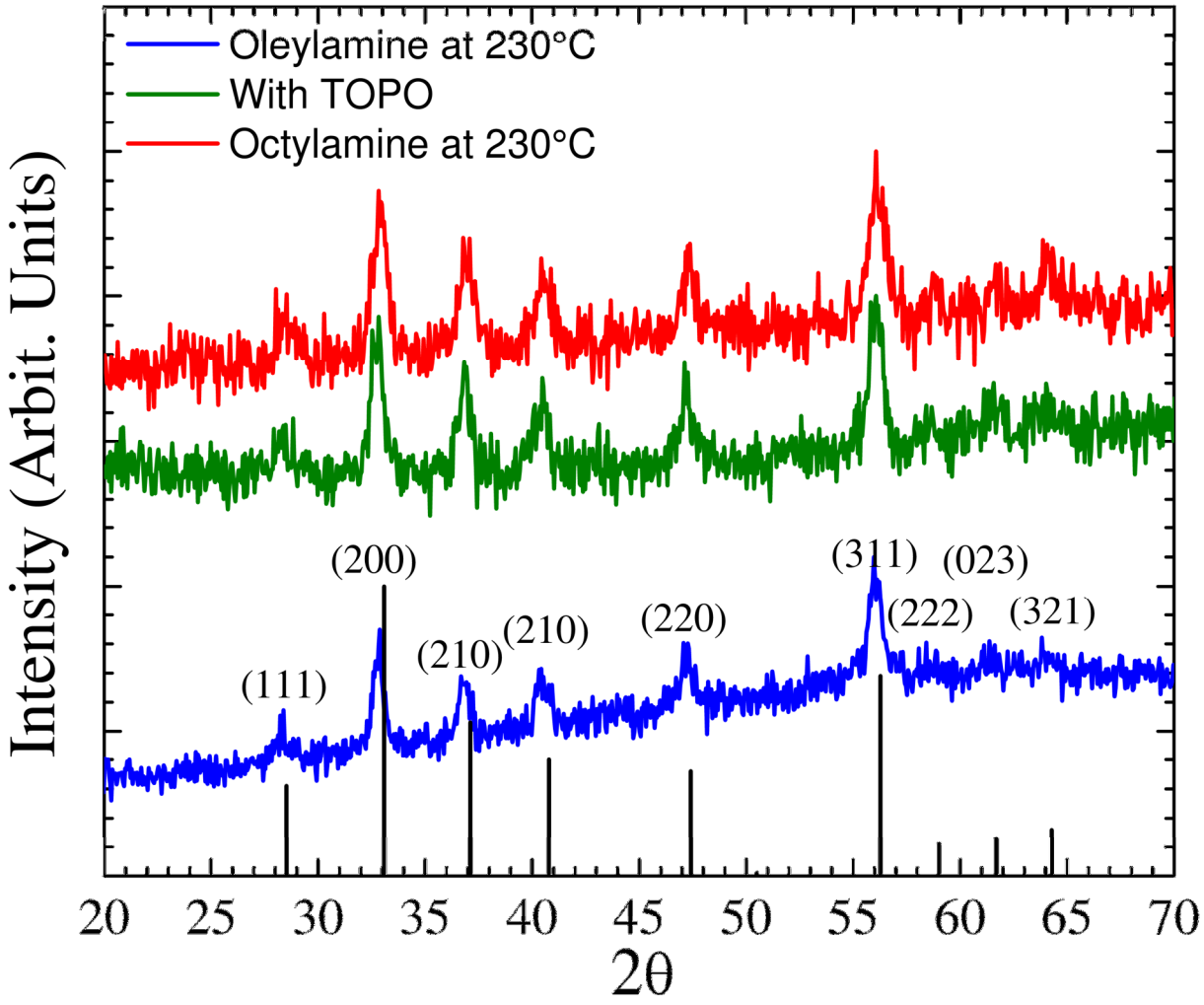

Fig. 3.16. The XRD spectra of iron pyrite nanocrystals with TOPO, octylamine at the synthetic temperature of 230°C, and the oleylamine sample where all three spectra match the vertical lines of the reference pattern.

(220), (311), (222), (023), and (321), respectively in the same manner as the samples with TOPO and the octylamine sample at 230°C. This has helped to confirm that the iron pyrite with oleylamine is phase-pure face-centered cubic iron pyrite nanocrystals. The lattice spacing is again calculated to be 0.27 nm, in accordance with the previous results for the lattice spacing and the lattice spacing of Wang et al. [11]. The only significant difference found between the three

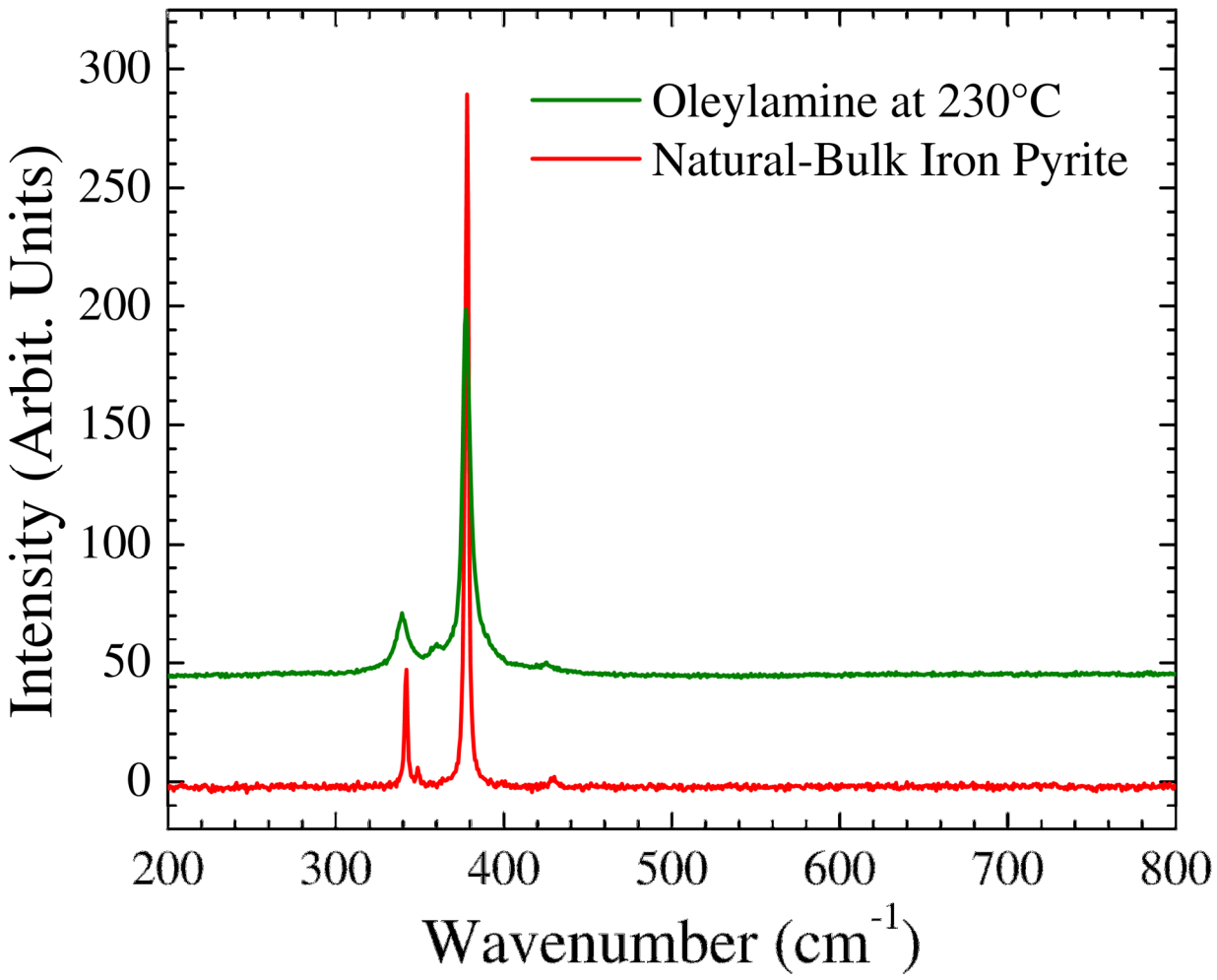

Fig. 3.17. The micro-Raman spectra of iron pyrite of both the natural-bulk iron pyrite as well as the synthesized iron pyrite nanocrystals with oleylamine.

samples from the XRD is the difference in the calculated grain size by the Scherrer formula. While the octylamine at 230°C and the sample with TOPO were calculated to have grain sizes of 8.8 and 13.4 nm, respectively, the oleylamine sample was calculated to have a larger grain size of 19.2 nm.

Micro-Raman has been used to compare the as synthesized iron pyrite nanocrystals with oleylamine to a natural-bulk sample of iron pyrite in Fig. 3.17, where the blue line represents the

synthesized iron pyrite nanocrystals while the red line represents the natural-bulk iron pyrite. The spectra for the iron pyrite natural-bulk and the synthesized iron pyrite exhibit two peaks for each sample, one at 340 cm^{-1} and the other is at 380 cm^{-1}. The main difference is the breadth of the peak, particularly noticeable is the difference in the peak at 340 cm^{-1}. For both peaks of the synthesized iron pyrite nanocrystals there is less intensity.

After using the HORIBA Scientific LabRAM HR to measure the micro-Raman it was then converted to measure the micro-PL with the given results shown in Fig. 3.18. The peak of the spectrum for the natural-bulk iron pyrite is at 810 nm while the peak for the synthesized iron pyrite nanocrystals with oleylamine is at 720 nm. This shift is likely caused by the difference in the nanocrystals grain size and the grain size of the natural-bulk iron pyrite. Due to the nature of the PL results where smaller grain size will lead to a peak shift towards lower wavelength. The other noticeable difference is the sharp edge around 700 nm caused by the limitations of the detector used for the measurements of the synthesized iron pyrite nanocrystals. The PL results lead to an approximate band gap of 1.72 eV for the synthesized iron pyrite nanocrystals, while the natural-bulk iron pyrite exhibits an approximate band gap of 1.53 eV.

Looking at the micro-Raman and the XRD spectra shows that the synthesized iron pyrite nanocrystals with oleylamine are phase-pure face-centered cubic iron pyrite nanocrystals. The UV-Vis-NIR absorption shows the direct band gap of the material is around 1.4 eV while the micro-PL showed a band gap closer to 1.72 eV. The difference in the measured direct band gap of the micro-PL and the UV-Vis absorption spectra is due to the shift in the peak of the micro-PL that is caused by the size of the nanocrystals, in a similar vein to how the peak was shifted from the natural-bulk iron pyrite compared to the synthesized nanocrystals. There is also a possibility

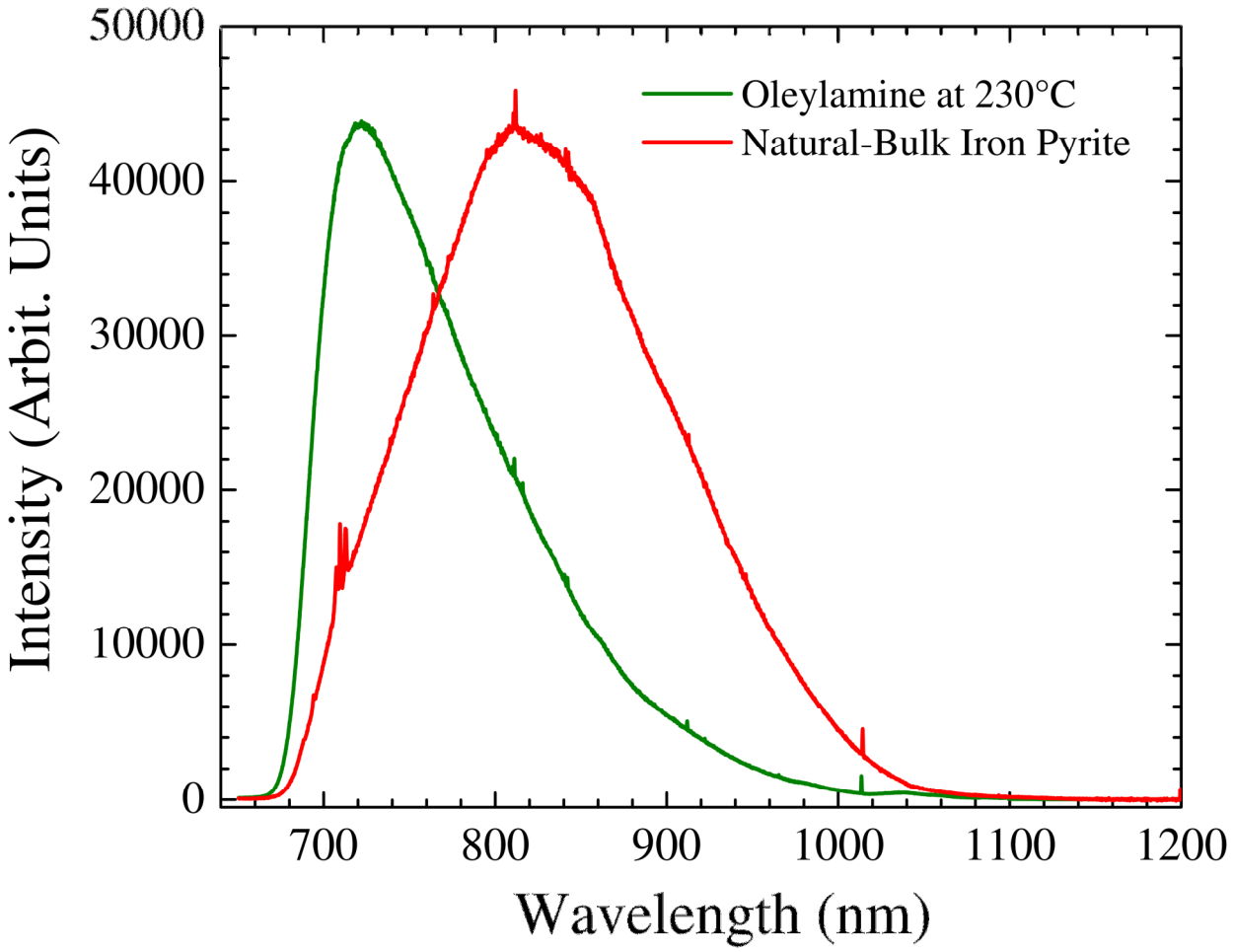

Fig. 3.18. The micro-PL spectra of iron pyrite of both the natural-bulk iron pyrite as well as the synthesized iron pyrite nanocrystals with oleylamine.

of a slight injection of oxygen as oxygen has been used to increase the band gap of iron pyrite by Hu et al. [17]. This slight injection of oxygen in the iron pyrite nanocrystals was shown in the EDX for the iron pyrite nanocrystals samples with and without TOPO in Fig. 3.11 and Fig. 3.13.

4. Conclusion and Future Work

Various iron pyrite nanocrystals were synthesized under a variety of conditions and characterized using SEM, TEM, EDX, micro-Raman, UV-Vis-NIR, and XRD. The iron pyrite nanocrystals synthesized with oleylamine as well as the nanocrystals synthesized with

octylamine for both the iron and sulfur precursor as well as the inclusion of TOPO produced the nanocrystals with the results closest to bulk face-centered cubic iron pyrite nanocrystals. The two samples both exhibited appropriate absorption characteristics for photovoltaic devices. Considering the two samples are roughly equal throughout it leads to the sample with oleylamine being slightly preferred because of the absence of TOPO. This is due to the possible effect that TOPO could have on a photovoltaic device in lowering the efficiency of said device.

The iron pyrite nanocrystals with oleylamine have been shown to be phase-pure face-centered iron pyrite nanocrystals by both XRD and micro-Raman. The usage of micro-PL has further proven the optoelectronic properties of the material and the possible usage for photovoltaic devices. Furthermore the larger grain size of the iron pyrite nanocrystals with oleylamine can help to exhibit larger carrier diffusion lengths and a smoother film that can help with the creation of various photovoltaic devices. With the synthesis of iron pyrite nanocrystals the possibility of making a photovoltaic device is possible by using a simple Schottky junction or a p-n junction solar cell device.

References

[1] T. Fukui, T. Miyadai, and S. Miyahara, "Photoconductivity of Natural Pyrite (FeS2)," *J. Phys. Soc. Jpn.*, vol. 31, pp. 1277, Oct. 1971.

[2] M. Birkholz, S. Fiechter, A. Hartmann, and H. Tributsch, "Sulfur deficiency in iron pyrite (FeS_{2-x}) and its consequences for band-structure models," *Phys. Rev. B*, vol. 43, pp. 11926-11936, May 1991.

[3] K. Büker, N. Alonso-Vante, and H. Tributsch, "Photovoltaic output limitation of *n*-FeS_2 (pyrite) Schottky barriers: A temperature-dependent characterization," *J. Appl. Phys.*, vol. 72, pp. 5721-5728, Dec. 1992.

[4] I. Opahle, K. Koepernik, and H. Eschrig, "Full-potential band-structure calculation of iron pyrite," *Phys. Rev. B*, vol. 60 pp. 14035-14041, Aug. 1999.

[5] S. Nakamura and A. Yamamoto, "Electrodeposition of pyrite (FeS_2) thin films for photovoltaic cells," *Sol. Energy Mater. And Sol. Cells*, vol. 65, pp. 79-85, Jan. 2001.

[6] N. Takahashi, Y. Nakatuni, T. Yatomi, and T. Nakamura, "Growth of Single-Crystal Pyrite Films by Atmospheric Pressure Chemical Vapor Deposition," *Chem. Mater.*, vol. 15, pp. 1763-1765, Apr. 2003.

[7] Y. Z. Dong, Y. F. Zheng, H. Duan, Y. F. Sun, and Y. H. Chen, "Formation of pyrite (FeS_2) thin nano-films by thermal-sulfurating electrodeposition films at different temperature," *Mater. Lett.*, vol. 59, pp. 2398-2402, Aug. 2005.

[8] A.P. Chandra and A.R. Gerson, "The mechanisms of pyrite oxidation and leaching: A fundamental perspective," *J. Surf. Rep.*, vol. 65, pp. 293-315, Sept. 2010.

[9] C. Wadia, A. P. Alivisatos, and D. M. Kammen, "Materials Availability Expands the Opportunity for Large-Scale Photovoltaics Deployment," *Environ. Sci. Technol.*, vol. 43 pp. 2072-2077, Feb. 2009.

[10] C. Wadia, Y. Wu, S. Gul, S.K. Volkman, J. Guo, and A.P. Alivisatos, "Surfactant-Assisted Hydrothermal Synthesis of Single phase Pyrite FeS_2 Nanocrystals," *Chem. Mater.*, vol. 21 pp. 2568-2570, June 2009.

[11] D.-W. Wang, Q.-H. Wang, and T.-M. Wang, "Controlled growth of pyrite FeS_2 crystallites by a facile surfactant-assisted solvothermal method," *CrystEngComm*, vol. 12, pp. 755-761, Mar. 2010.

[12] J. Puthussery, S. Seefeld, N. Berry, M. Gibbs, and M. Law, "Colloidal Iron Pyrite (FeS_2) Nanocrystal Inks for Thin-Film Photovoltaics," *J. Am. Chem. Soc.*, vol. 133, pp. 716-719, Feb. 2011.

[13] Y. Bi, Y. Yuan, C.L. Exstrom, S.A. Darveau, and J. Huang, "Air Stable, Photosensitive, Phase Pure Iron Pyrite Nanocrystal Thin Films for Photovoltaic Application," *Nano Lett.*, vol. 11, pp. 4953-4957, Nov. 2011.

[14] T. Unold and H. W. Schock, "Nonconventional (Non-Silicon-Based) Photovoltaic Materials," *Annu. Rev. Mater. Res.*, vol. 41 pp. 297-321, Aug. 2011.

[15] M. Cabán-Acevedo, M. S. Faber, Y. Tan, R. J. Hamers, and S. Jin, "Synthesis and Properties of Semiconducting Iron Pyrite (FeS_2) Nanowires," *Nano Lett.*, vol. 12, pp. 1977-1982, Apr. 2012.

[16] J. Hu, Y. Zhang, M. Law, and R. Wu, "First-principles studies of the electronic properties of native and substitutional anionic defects in bulk iron pyrite," *Phys. Rev. B*, vol. 85, pp. 085203, Feb. 2012.

[17] J. Hu, Y. Zhang, M. Law, and R. Wu, "Increasing the Band Gap of Iron Pyrite by Alloying with Oxygen," *J. Am. Chem. Soc.*, vol. 134, pp. 13216-13219, Aug. 2012.

[18] D.-Y. Wang, Y.-T. Jiang, C.-C. Lin, S.-S. Li, Y.-T. Wang, C.-C. Chen, and C.-W. Chen, "Solution-Processable Pyrite FeS_2 Nanocrystals for the Fabrication of Heterojunction Photodiodes with Visible to NIR Photodetection," *Adv. Mater.*, vol. 24, pp. 3415-3420, Jul. 2012.

[19] Y.N. Zhang, J. Hu, M. Law, and R.Q. Wu, "Effect of surface stoichiometry on the band gap of the pyrite FeS_2 (100) surface," *Phys. Rev. B*, vol. 85, pp. 085314, Feb. 2012.

[20] L. Zhu, B. Richardson, J. Tanumihardja, and Q. Yu, "Controlling morphology and phase of pyrite FeS_2 hierarchical particles *via* the combination of structure-direction and chelating agents," *CrystEngComm*, vol. 12, pp. 4188-4195, Dec. 2012.

[21] S.-C. Hsiao, C.-M. Hsu, S.-Y. Chen, Y.-H. Perng, Y.-L. Chueh, L.-J. Chen, and L.-H. Chou, "Facile synthesis and characterization of high temperature phase FeS_2 pyrite nanocrystals," *Mater. Lett.*, vol. 75, pp. 152-154, May 2012.

[22] W. Shockley and H.J. Queisser, "Detailed Balance Limit of Efficiency of *p-n* Junction Solar Cells," *J. Appl. Phys.*, vol. 32, pp. 510-519, Mar. 1961.

[23] J. Jiao, L. Chen, D. Kuang, W. Gao, H. Feng, and J. Xia, "Synthesis of FeS and Co-doped FeS_2 films with the aid of supercritical carbon dioxide and their photoelectrochemical properties," *RSC Adv.*, vol. 1, pp. 255-261, Aug. 2011.

[24] D. Rickard and G.W. Luther III, "Chemistry of Iron Sulfides," *Chem. Rev.*, vol. 107, pp. 514-562, Feb. 2007.

[25] D.M. Chapin, C.S. Fuller, and G.L. Pearson, "A New Silicon pn Junction Photocell for Converting Solar Radiation into Electrical Power," *J. Appl. Phys.*, vol. 25, pp. 676-677,

May 1954.

[26] J.-T. Shieh, C.-H. Liu, H.-F. Meng, S.-R. Tseng, Y.-C. Chao, and S.-F. Horng, "The effect of carrier mobility in organic solar cells," *J. Appl. Phys.*, vol. 107, pp. 084503, Apr. 2010.

[27] C. de Mello Donegá, P. Liljeroth, and D. Vanmaekelbergh, "Physicochemical Evaluation of the Hot-Injection Method, a Synthesis Route for Monodisperse Nanocrystals," *Small*, vol. 1, pp. 1152-1162, Dec. 2005.

[28] A.L. Patterson, "The Scherrer Formula for X-Ray Particle Size Determination," *Phys. Rev.*, vol. 56, pp. 978-982, Nov. 1939.